
MEDMAMBA: VISION MAMBA FOR MEDICAL IMAGE CLASSIFICATION

Yubiao Yue

School of Biomedical Engineering
Guangzhou Medical University
jiche2020@126.com

Zhenzhang Li

School of Mathematics and Systems Science
Guangdong Polytechnic Normal University
zhenzhangli@gpnu.edu.cn

ABSTRACT

Since the era of deep learning, convolutional neural networks (CNNs) and vision transformers (ViTs) have been extensively studied and widely used in medical image classification tasks. Unfortunately, CNN's limitations in modeling long-range dependencies result in poor classification performances. In contrast, ViTs are hampered by the quadratic computational complexity of their self-attention mechanism, making them difficult to deploy in real-world settings with limited computational resources. Recent studies have shown that state space models (SSMs) represented by Mamba can effectively model long-range dependencies while maintaining linear computational complexity. Inspired by it, we proposed MedMamba, the first Vision Mamba for generalized medical image classification. Concretely, we introduced a novel hybrid basic block named SS-Conv-SSM, which purely integrates the convolutional layers for extracting local features with the abilities of SSM to capture long-range dependencies, aiming to model medical images from different image modalities efficiently. By employing the grouped convolution strategy and channel-shuffle operation, MedMamba successfully provides fewer model parameters and a lower computational burden for efficient applications without sacrificing accuracy. We thoroughly evaluated MedMamba using 16 datasets containing ten imaging modalities and 411,007 images. Experimental results show that MedMamba demonstrates competitive performance on most tasks compared with the state-of-the-art methods. This work aims to explore the potential of Vision Mamba and establish a new baseline for medical image classification, thereby providing valuable insights for developing more powerful Mamba-based artificial intelligence algorithms and applications in medicine. The source codes and all pre-trained weights of MedMamba are available at <https://github.com/YubiaoYue/MedMamba>.

Keywords Medical Image Classification · Deep learning · State Space models · Vision Mamba

1 Introduction

Medical image classification is a basic step in medical image analysis and has been an essential task in computer-aided diagnosis (CAD) [1]. It aims to distinguish medical images according to certain criteria (such as clinical pathology or imaging patterns) and plays a vital role in the field of healthcare, including clinical diagnosis, disease treatment, and disease monitoring [2, 3, 4, 5, 6]. Benefitting from the rapid development of digital medical imaging technology, a large number of medical images from different imaging modalities, including computed tomography (CT), ultrasound (US), X-ray, microscope, endoscope, and magnetic resonance imaging (MRI), have been widely used, greatly facilitating the development of clinical medicine [7]. However, the tremendous increase in medical images poses a challenge for manual classification and interpretation, as this process is very time-consuming and labor-intensive [8, 9]. Particularly, the ability of clinicians (such as sonographers, radiologists, and pathologists) to accurately distinguish images of various organs and lesions largely depends on their domain knowledge and clinical experience. This reliance leads to significant differences in the methods adopted and conclusions drawn by different individuals when analyzing and interpreting medical images [10].

To address this clinical challenge, many Artificial Intelligence-based CAD solutions have been developed and tested to improve the accuracy and efficiency of disease diagnosis and management [11, 12]. Over the past few decades, the

technology used in CAD has undergone a transformation from traditional machine learning to deep learning. Due to the explosive growth in the number of medical images and the significant improvement in computing device performance, deep learning models has achieved tremendous success and shown great promise in medical image processing tasks. Nowadays, how to employ deep learning technology to effectively perform various medical image classification tasks has become a fundamental and significant task in CAD and computer vision [13, 14, 15]. Importantly, an excellent medical image classification model can also serve as a generic vision backbone to effectively extract representative features from various advanced tasks, such as medical image segmentation, medical image object detection, and medical image reconstruction [16].

The two most popular architectures in deep learning, namely convolutional neural networks (CNNs) and vision transformers (ViTs), are dominating the field of visual representation learning and have been widely used in various image classification tasks [17, 18, 19]. It is worth noting that compared with natural image datasets (e.g., ImageNet [20]), the intra-class variability and inter-class similarity pose an even greater challenge for medical image classification [21]. Although CNNs can effectively extract local features, they have difficulty in capturing global context and long-range dependencies, leading to insufficient feature extraction and unsatisfactory classification results, as they are inherently limited by their local receptive field. ViTs, originally designed for natural language processing, have been successfully applied to computer vision tasks. In essence, ViTs are not able to handle spatial image hierarchies but represent an input image as a sequence of image patches [22]. By adopting cascaded self-attention modules, vision transformers can effectively capture long-range dependencies, but unfortunately, this degrades local feature details [23, 24]. Recent studies have shown that combining local features in an image with corresponding long-range dependencies is the key to achieving accurate medical image classification results [25, 26, 27, 28, 29]. Given this complementarity between CNNs and ViTs and the characteristics of medical images, researchers have begun to utilize hybrid architectures based on CNN and ViT (CNN-ViT) to more efficiently analyze various medical images [30, 31, 32, 33, 34]. The only drawback is that the self-attention mechanism of ViT has high quadratic complexity in long sequence modeling, resulting in a high computational burden (especially for medical images with high resolution) and making it difficult to deploy the model in clinical settings with limited computing resources. Some previous works have attempted to use CNN, ViT and CNN-ViT to build a generic medical image classification model [9, 15, 16, 21, 35, 36]. However, these models have more or less the above limitations. Given the importance of medical image classification tasks and the limitations of existing models, exploring a generic medical image classification architecture that can achieve a good trade-off between visual representation learning capabilities and computing resource consumption is of great significance for the development of intelligent clinical diagnosis systems and computer vision.

Recently, structured state-space models (SSMs) [37, 38] inspired by classical state-space models have attracted great attention due to their computational efficiency and excellent performance in modeling long-range dependencies. Essentially, these models can be interpreted as a combination of recurrent neural networks (RNNs) and convolutional neural networks (CNNs) and can be computed very efficiently as either a recurrence or convolution, with linear or near-linear scaling in sequence length. Notably, Mamba [39], a state-of-the-art selective structured state space model, addresses the inherent limitations of previous SSMs, successfully demonstrates their efficiency and effectiveness in long sequence modeling, and achieves cutting-edge performance in continuous long sequence data analysis such as natural language processing and genomic analysis [40]. From the perspective of internal mechanisms, Mamba incorporates time-varying parameters into the SSM and employs a novel hardware-aware algorithm to enable very efficient training and inference [41]. Crucially, it avoids the high quadratic computational complexity caused by the self-attention mechanism. Several recent studies have preliminarily explored the effectiveness of SSMs in various visual tasks, such as ImageNet classification[41, 42], remote sensing image classification [43], image dehazing [44], point cloud analysis[45], and medical image segmentation[40, 46, 47, 48]. However, the potential of SSM in classifying medical images with different imaging modalities and morphological differences has not been fully studied. Given the impressive efficiency and powerful long-range dependency modeling capabilities of SSM, we attempted to employ SSM to replace Transformer to capture long-range dependencies in medical images efficiently. More precisely, we intuitively proposed a novel SSM-based generalized medical image classification model named MedMamba. Without too many fancy designs, MedMamba purely utilizes classic convolutional layers and SSM layers to extract local and global features of medical images from different modalities, respectively. By introducing the classic ideas of grouped convolution and channel-shuffle, MedMamba successfully provides fewer parameters and lower FLOPs for efficient medical artificial intelligence applications while maintaining excellent performance.

In summary, the contributions of this work can be summarized as follows: 1) To the best of our knowledge, this is the first research work that attempts to apply SSM to generalized medical image classification tasks and validates its effectiveness. 2) We proposed a novel hybrid basic block named SS-Conv-SSM. SS-Conv-SSM integrates channel-split, convolutional layers, SSM layers, and channel-shuffle to enables the model to extract features at all levels in medical images more efficiently. By repeatedly stacking SS-Conv-SSM block, the first vision Mamba for medical image classification, MedMamba, is introduced, including three variants (MedMamba-Tiny, MedMamba-Small, and

MedMamba-Base). 3) 16 datasets with ten imaging modalities and 411,007 images and multiple performance metrics are used to evaluate MedMamba comprehensively. We fully observed the performance of SSM-based models on medical image datasets with different modalities and different data sizes. 4) We compared MedMamba with numerous state-of-the-art generic visual backbone networks. Experimental results show that MedMamba achieves competitive performance in various tasks. 5) We used t-SNE, Grad-CAM, and robustness analysis strategy to enhance the transparency and credibility of MedMamba, helping application developers and healthcare personnel to better understand and trust the model’s decision-making process and facilitate the practical application of MedMamba. 6) Extensive experiments have demonstrated that the hybrid architecture based on convolution and SSM is more efficient in modeling medical images, laying a solid foundation for the design of future Mamba-based models for medical imaging.

2 Related work

Convolution Neural Networks. Convolutional Neural Network (CNN) is one of the most significant deep learning networks. The research on CNNs began in the 1980s and 1990s. Time Delay Neural Network [49] and LeNet-5 [50] were the earliest convolutional neural networks. After the 21st century, with the introduction of deep learning theory and improved numerical computing equipment, CNNs represented by AlexNet [51], Vgg [52], and ResNet [53] have made significant breakthroughs in visual recognition tasks. The inspiration for CNN comes from the natural visual perception mechanism of living creatures, which enables them to automatically and effectively learn spatial hierarchical features from image data, making it suitable for various image recognition tasks [54, 55]. With the help of powerful computing devices (GPUs) and large-scale datasets, increasingly efficient CNNs have been proposed to enhance the practicality of AI systems in different scenarios [56, 57, 58, 59, 60]. In the medical field, CNNs can learn and extract meaningful features from complex medical images and are widely used in skin disease diagnosis, cancer detection, histopathological analysis, infectious disease control, retinal disease identification, etc. [61, 62, 63, 64, 65]. Utilizing well-designed CNNs for ImageNet and transfer learning strategies has become a common practice in medical image classification tasks. Today, CNN-based CAD can help doctors make more accurate diagnoses and improve patient treatment plans. With future technological advances and the continuously increasing medical data, CNNs will play an increasingly important role in improving the accuracy, efficiency, and automation of medical image analysis, opening up new possibilities for precision medicine and early diagnosis [66].

Vision Transformers. Vision Transformer (ViT) is a deep learning model based on a self-attention mechanism, initially introduced by Google Research in 2020 for image recognition tasks [67]. Unlike traditional CNNs, ViTs divide images into multiple patches and process them as sequences. This approach draws on the success of the Transformer model in the field of natural language processing. The proposal of ViTs marks a shift in deep learning models from relying on convolutional operations to utilizing self-attention mechanisms to process images. Early ViT-based models typically required large-scale datasets and appeared in simple configurations [68]. Recent research on model design tends to incorporate inductive biases in visual perception into ViTs [69, 70, 71, 72, 73]. In the medical field, ViTs are widely used in various tasks, such as medical image classification, medical image registration, and medical image segmentation, due to their ability to capture long-range dependencies and flexibly process images of different sizes [15, 34, 36, 74, 75]. Since ViTs implement modality-agnostic modeling by treating an image as a sequence of patches without 2D inductive bias, it has become the preferred architecture for multimodal applications [41]. At the same time, driven by the continuous growth of datasets, the increase in model size, and the advancement of model architecture, ViT-based foundation models provide unprecedented capabilities and are flexibly applied by researchers to multiple downstream tasks in the medical field [76, 77]. For example, researchers proposed MedSAM to segment everything in medical images [78]. In contrast, RETGround has been proposed to identify and diagnose various diseases in the field of ophthalmology [79]. In addition, UNI and PLIP are used to improve computational pathology [80, 81]. With more targeted improvements and optimizations, ViT is expected to play a greater role in medical image analysis.

Visual State Space Models. State Space Model (SSM) is a mathematical model used to describe and analyze the behavior of dynamic systems. Due to the need for a large amount of computation and memory, early SSMs were difficult to train and were not widely used in practice. Structured State Space Sequence Model (S4) [37] employs a Normal Plus Low-Rank (NPLR) representation to efficiently compute the convolution kernel by leveraging the Woodbury identity for matrix inversion, addressing these limitations. As standalone sequence transformations, SSMs can be incorporated into end-to-end neural network architectures. Since then, various variants of SSMs have emerged [82, 83, 84]. Unfortunately, the constant sequence transformation in SSM limits their context-based reasoning ability. Recent Mamba (Selective SSM) merges time-varying parameters into SSMs and formulates a hardware-aware algorithm for efficient training and inference [39], effectively enhancing the potential of SSMs. With the success of SSMs in long sequence modeling, researchers have begun to attempt to apply it to computer vision tasks, just like using the Transformer originally designed for NLP. ViS4mer [85] and S4ND [86] introduced the SSM blocks to facilitate modeling visual data across 1D, 2D, and 3D. VMamba [42] proposed a pioneer vision backbone that integrates a cross-scan module with a mamba

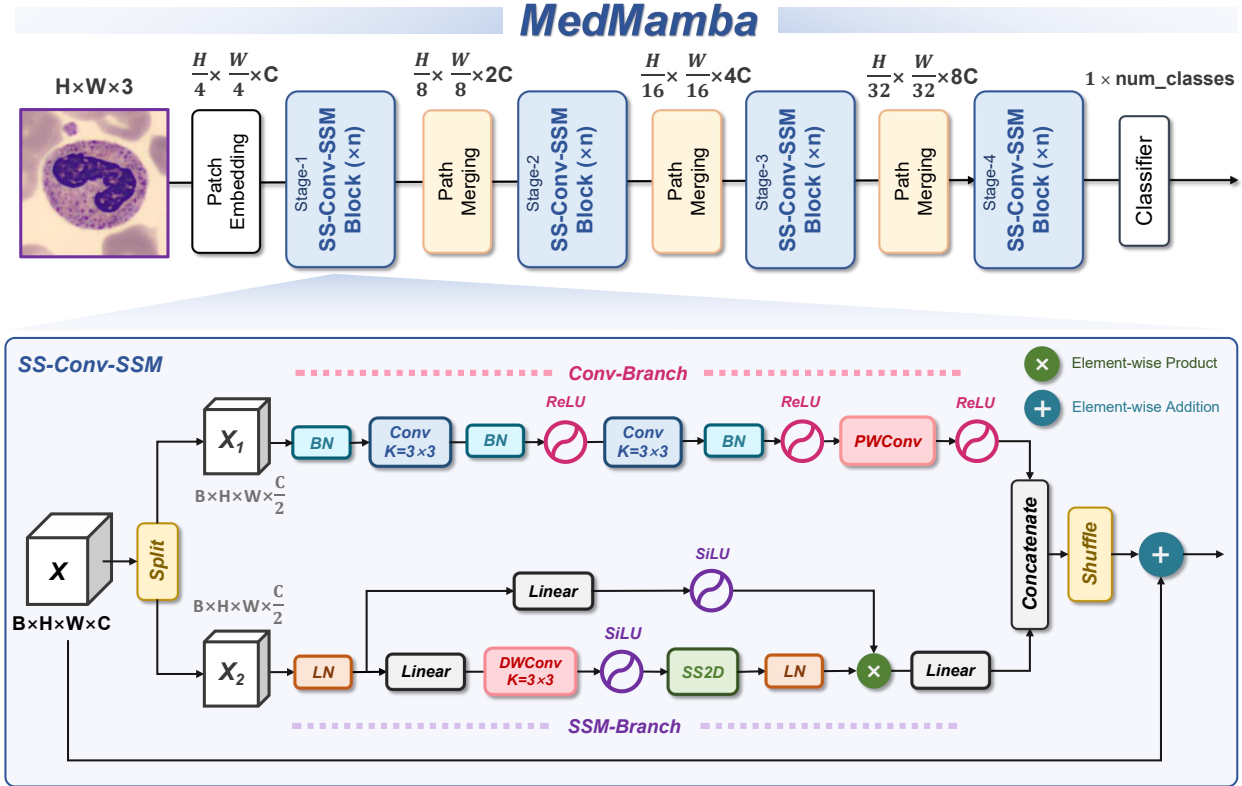


Figure 1: The overall architecture of the MedMamba. BN, LN, Linear, PWConv and DWConv represent Batch normalization, layer normalization, Linear layer, Point-wise convolution and Depth-wise convolution, respectively.

module to address the direction-sensitive problem arising from the differences between 1D sequences and 2D images. Similarly, Vim [41] proposed bidirectional SSM for data-dependent global visual context modeling and incorporates position embeddings for location-aware visual understanding. Due to Mamba’s impressive performance in visual tasks, researchers are actively applying Mamba to various fields. In the field of medical imaging, U-Mamba [48] attempted to integrate Mamba layers into the encoder of nnUNet to enhance the modeling ability of CNN for long-range dependencies, and proposed a general-purpose network for both 3D and 2D biomedical image segmentation. Meanwhile, SegMamba [47] combines the U-shape structure with Mamba to model the whole volume of global features at various scales. In addition, VM-UNet [46] constructed the first medical image segmentation model based on a pure SSM-based model, establishing a new baseline for medical image segmentation. Swin-UMamba [40] revealed how to enhance Mamba’s performance in medical image segmentation using ImageNet-based training. The above studies demonstrate the promising results of SSM-based deep learning models in visual tasks.

3 Methods

In this section, we started by introducing the preliminary concepts related to MedMamba, i.e., the state space models and the discretization process. We then presented a comprehensive discussion for the overall architecture of MedMamba and the 2D-Selective-Scan mechanism. Finally, we provided detailed modelling process of the SS-Conv-SSM block which serves as the core element of MedMamba.

3.1 Preliminaries

The recent SSM-based models, i.e., Structured State Space Sequence Models (S4) and Mamba, rely on a classical continuous system that maps a one-dimensional input function or sequence, denoted as $x(t) \in \mathcal{R}$, through intermediate implicit states $h(t) \in \mathcal{R}^N$ to an output $y(t) \in \mathcal{R}$. The aforementioned process can be represented as a linear Ordinary Differential Equation (ODE) [39, 41, 42, 46]:

$$\begin{aligned} h'(t) &= \mathbf{A}h(t) + \mathbf{B}x(t) \\ y(t) &= \mathbf{C}h(t) \end{aligned} \quad (1)$$

where $\mathbf{A} \in \mathcal{R}^{N \times N}$ represents the state matrix, while $\mathbf{B} \in \mathcal{R}^{N \times 1}$ and $\mathbf{C} \in \mathcal{R}^{N \times 1}$ denote the projection parameters.

The S4 model and Mamba discretize the continuous system to make it more suitable for deep learning. Specifically, they introduce a timescale parameter Δ to transform \mathbf{A} and \mathbf{B} into discrete parameters $\overline{\mathbf{A}}$ and $\overline{\mathbf{B}}$ using a fixed discretization rule. Typically, the zero-order hold (ZOH) is employed as the discretization rule and can be defined as follows:

$$\begin{aligned} \overline{\mathbf{A}} &= \exp(\Delta \mathbf{A}) \\ \overline{\mathbf{B}} &= (\Delta \mathbf{A})^{-1}(\exp(\Delta \mathbf{A}) - \mathbf{I}) \cdot \Delta \mathbf{B} \end{aligned} \quad (2)$$

After discretization, Equation 1 utilizing a step size Δ can be redefined as follows:

$$\begin{aligned} h'(t) &= \overline{\mathbf{A}}h(t) + \overline{\mathbf{B}}x(t) \\ y(t) &= \mathbf{C}h(t) \end{aligned} \quad (3)$$

At the end of the process, the SSM model employ a global convolution to calculate the output:

$$\begin{aligned} \overline{\mathbf{K}} &= (\mathbf{C}\overline{\mathbf{B}}, \mathbf{C}\overline{\mathbf{A}}\overline{\mathbf{B}}, \dots, \mathbf{C}\overline{\mathbf{A}}^{L-1}\overline{\mathbf{B}}) \\ y &= x * \overline{\mathbf{K}} \end{aligned} \quad (4)$$

where $\overline{\mathbf{K}} \in \mathcal{R}^L$ represents a structured convolutional kernel, and L denotes the length of the input sequence x .

3.2 MedMamba

3.2.1 Overall architecture

Figure 1 shows the overall architecture of MedMamba. Specifically, MedMamba includes a patch embedding layer, stacked SS-Conv-SSM blocks, patch merging layers for down-sampling, and a feature classifier.

Similar to typical ViTs, MedMamba first partitions the input image $x \in R^{H \times W \times 3}$ into non-overlapping patches of size 4×4 using a patch embedding layer, subsequently mapping the channel dimensions of the image to C , but without further flattening the patches into a 1-D sequence. Patch embedding layer results in a feature map with $\frac{H}{4} \times \frac{W}{4} \times C$ without damaging the 2D structure of the input image.

Subsequently, MedMamba repeatedly stacks SS-Conv-SSM blocks to build Stage-1 that further process the feature map without changing the dimension size of it. To construct hierarchical representations, MedMamba utilizes a patch merging layer to down-sampling the feature map. Stage-2, Stage-3 and Stage-4 repeat the above process, and two patch merging layers are used for down-sampling the outputs of Stage-2 and Stage-3, resulting in two outputs with resolutions of $\frac{H}{16} \times \frac{W}{16} \times 4C$ and $\frac{H}{32} \times \frac{W}{32} \times 8C$, respectively. At the end of the network, a classic classifier consisting of an adaptive global pooling layer and a linear layer is used to calculate the category of the input image. The entire process of MedMamba processing input is similar to the popular CNNs and ViTs. Besides, the default size for MedMamba's input is set as $224 \times 224 \times 3$.

Like the configuration of most ViTs, three different scales of MedMamba were developed, i.e., MedMamba-Tiny, MedMamba-Small, and MedMamba-Base (referred to as MedMamba-T, MedMamba-S, and MedMamba-B, respectively). Detailed architectural specifications are outlined in Table 1. The FLOPs for all models are assessed using a 224×224 input size.

3.2.2 2D-selective-scan

The 2D-selective-scan (SS2D) (Figure 2) proposed by VMamba[42] is one of the core elements of MedMamba. SS2D inherits the selective scan space state sequence model (S6) designed for natural language processing tasks and successfully solves the "direction-sensitive" problem in S6. Specifically, to narrow the gap between 1-D array scanning and 2-D plain traversing, SS2D introduced a Cross-Scan Module (CSM), facilitating the extension of S6 to visual data without affecting the reception field. CSM adopts a four-way scanning strategy, i.e., from four corners all across the feature map to the opposite location to traverse the spatial domain of image feature maps, which ensures that each pixel in a feature map integrates information from all other locations in different directions, resulting in a global receptive field without increasing the linear computational complexity.

Layer name	Output Size	MedMamba-Tiny	MedMamba-Small	MedMamba-Base
Patch-E	56×56	conv 4×4, 96, stride 4 Channel number → 96	conv 4×4, 96, stride 4 Channel number → 96	conv 4×4, 128, stride 4 Channel number → 128
Stage 1	56×56	$\begin{bmatrix} \text{Channel Split} \\ \text{Conv-SSM} \\ \text{Channel Concat} \\ \text{Channel Shuffle} \end{bmatrix} \times 2$	$\begin{bmatrix} \text{Channel Split} \\ \text{Conv-SSM} \\ \text{Channel Concat} \\ \text{Channel Shuffle} \end{bmatrix} \times 2$	$\begin{bmatrix} \text{Channel Split} \\ \text{Conv-SSM} \\ \text{Channel Concat} \\ \text{Channel Shuffle} \end{bmatrix} \times 2$
Path-M	28×28	Channel number → 192		Channel number → 256
Stage 2	28×28	$\begin{bmatrix} \text{Channel Split} \\ \text{Conv-SSM} \\ \text{Channel Concat} \\ \text{Channel Shuffle} \end{bmatrix} \times 2$	$\begin{bmatrix} \text{Channel Split} \\ \text{Conv-SSM} \\ \text{Channel Concat} \\ \text{Channel Shuffle} \end{bmatrix} \times 2$	$\begin{bmatrix} \text{Channel Split} \\ \text{Conv-SSM} \\ \text{Channel Concat} \\ \text{Channel Shuffle} \end{bmatrix} \times 2$
Path-M	14×14	Channel number → 384		Channel number → 512
Stage 3	14×14	$\begin{bmatrix} \text{Channel Split} \\ \text{Conv-SSM} \\ \text{Channel Concat} \\ \text{Channel Shuffle} \end{bmatrix} \times 4$	$\begin{bmatrix} \text{Channel Split} \\ \text{Conv-SSM} \\ \text{Channel Concat} \\ \text{Channel Shuffle} \end{bmatrix} \times 8$	$\begin{bmatrix} \text{Channel Split} \\ \text{Conv-SSM} \\ \text{Channel Concat} \\ \text{Channel Shuffle} \end{bmatrix} \times 12$
Path-M	7×7	Channel number → 768		Channel number → 1024
Stage 4	7×7	$\begin{bmatrix} \text{Channel Split} \\ \text{Conv-SSM} \\ \text{Channel Concat} \\ \text{Channel Shuffle} \end{bmatrix} \times 2$	$\begin{bmatrix} \text{Channel Split} \\ \text{Conv-SSM} \\ \text{Channel Concat} \\ \text{Channel Shuffle} \end{bmatrix} \times 2$	$\begin{bmatrix} \text{Channel Split} \\ \text{Conv-SSM} \\ \text{Channel Concat} \\ \text{Channel Shuffle} \end{bmatrix} \times 2$
Classifier	1×1	Adaptive global pooling, Linear (768/1024->num-classes), Softmax		
Parameter Size(M)		15.2	23.5	48.1
FLOPs(G)		2.0×10^9	3.5×10^9	7.4×10^9

Table 1: **Architectural overview of the MedMamba variants.** Patch-E and Patch-M represents Patch-Embedding and Patch-Merging, respectively. The results for parameter size and FLOPs are calculated when the number of classes is equal to 1000.

By integrating CSM, SS2D inherits the linear complexity of S6 while capturing long-range dependencies, which is essential for achieving accurate medical image classification. The SS2D contains three components consists: a scan expanding operation (CSM), an S6 block, and a scan merging operation. Figure2 visually presents the internal mechanism of SS2D. Concretely, the scan expanding operation first unfolds the input image along four different directions (top-left to bottom-right, bottom-right to top-left, top-right to bottom-left, and bottom-left to top-right) into sequences. An S6 block then processes all sequences to extract the features, ensuring that information from various directions is thoroughly scanned. Lastly, the four output features from the four directions are merged through scan merging to construct the final 2D feature map, resulting in a final output of the same size as the input.

The S6 block originates from Mamba and introduces a selective mechanism based on S4 by adjusting the parameters of SSM according to input. This enables the model to distinguish and retain relevant information while filtering out irrelevant information. The pseudo-code for the S6 block is presented in Algorithm 1.

For ease of understanding, we denoted the input of SS2D, i.e., the feature map, as $I \in R^{H \times W \times C}$, where $I[h][w]$ represents one token in the h-th row and w-th column of the feature map. Therefore, the scan expanding operation can be formalized as follows[87]:

$$s_1[i] = I[i \bmod W][\lfloor i/W \rfloor] \quad (5)$$

$$s_2[i] = I[(N - i - 1) \bmod W][\lfloor (N - i - 1)/W \rfloor] \quad (6)$$

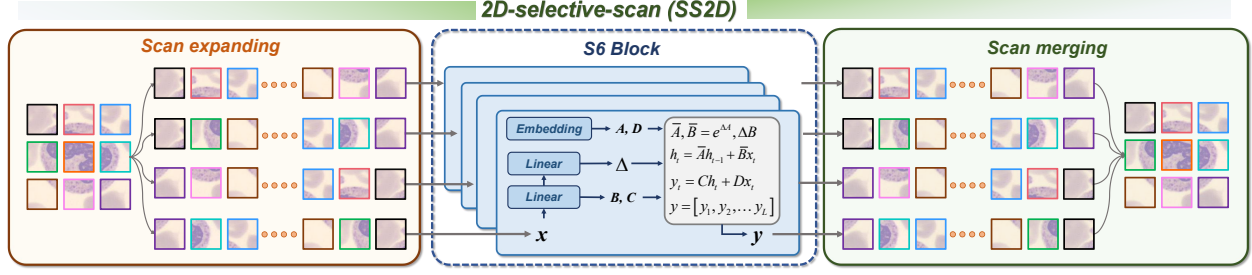


Figure 2: Visual display of the internal modeling process of SS2D.

Algorithm 1 Pseudo-code for S6 block in SS2D [39, 41, 42, 46]

Input: x , the feature with shape $[B, L, D]$ (batch size, token length, dimension)

Params: \mathbf{A} , the nn.Parameter; \mathbf{D} , the nn.Parameter

Operator: $\text{Linear}(\cdot)$, the linear projection layer

Output: y , the feature with shape $[B, L, D]$

- 1: $\Delta, \mathbf{B}, \mathbf{C} = \text{Linear}(x), \text{Linear}(x), \text{Linear}(x)$
- 2: $\bar{\mathbf{A}} = \exp(\Delta \mathbf{A})$
- 3: $\bar{\mathbf{B}} = (\Delta \mathbf{A})^{-1} (\exp(\Delta \mathbf{A}) - \mathbf{I}) \cdot \Delta \mathbf{B}$
- 4: $h_t = \bar{\mathbf{A}} h_{t-1} + \bar{\mathbf{B}} x_t$
- 5: $y_t = \mathbf{C} h_t + \mathbf{D} x_t$
- 6: $y = [y_1, y_2, \dots, y_t, \dots, y_L]$
- 7: **return** y

$$s_3[i] = I[\lfloor i/H \rfloor][\lfloor i \bmod H \rfloor] \quad (7)$$

$$s_4[i] = I[\lfloor (N-i-1)/H \rfloor][\lfloor (N-i-1) \bmod H \rfloor] \quad (8)$$

Where $N = H \times W$, $0 \leq i < N$, $s_1, s_2, s_3, s_4 \in R^{N \times C}$ are the expanded and flattened token sequences. Next, we employed the S6 to selectively scan each token sequence, resulting in contextual token sequences $s'_1, s'_2, s'_3, s'_4 \in R^{N \times C}$. Immediately after, SS2D apply reversed operations to the contextual token sequences:

$$I'_1[i][j] = s'_1[j \times W + i] \quad (9)$$

$$I'_2[i][j] = s'_2[N - 1 - j \times W - i] \quad (10)$$

$$I'_3[i][j] = s'_3[i \times H + j] \quad (11)$$

$$I'_4[i][j] = s'_4[N - 1 - i \times H - j] \quad (12)$$

Where $I'_1, I'_2, I'_3, I'_4 \in R^{H \times W \times C}$ denote the expanded and transformed feature map of I . In the end, SS2D applies the scan merging to obtain the output:

$$I' = I'_1 + I'_2 + I'_3 + I'_4 \quad (13)$$

3.2.3 SS-Conv-SSM Block

A grouped convolution uses a group of convolutions (multiple kernels per layer) to promote the model to learn various high- and low-level features. This concept was first introduced in AlexNet [51] to distribute the model over multiple GPUs as an engineering compromise. In recent years, some studies have found that this module can be used to improve model performance while reducing model parameter size and model complexity. In order to enable MedMamba to model medical images more efficiently, we introduced this classic concept in the proposed SS-Conv-SSM. As a fundamental component of MedMamba, SS-Conv-SSM is a lightweight dual-branch block (Figure 2). It uses channel-split to partition the feature map into two groups and then uses Conv-Branch and SSM-Branch to extract global-local information from each group, respectively. Finally, SS-Conv-SSM employs channel-concatenation to restore the size of the channel dimension, while channel-shuffle is used to shuffle the feature map on the channel dimension to avoid information loss between channels caused by grouped convolution operations [59, 88]. We followed the settings of classic CNNs and ViTs and set the activation functions in Conv-Branch and SSM-Branch to ReLU [89] and SilU [90], respectively.

We formalized the modeling process of SS-Conv-SSM for the feature maps. Given a module input $x \in R^{H \times W \times C}$ and a module output $y \in R^{H \times W \times C}$, we used f to represent the channel-split, and then there is

$$x \in R^{H \times W \times C} x_{i=1,2} \in R^{H \times W \times \frac{C}{2}}$$

Next, the f^{-1} and g are used to represent channel-concatenation and channel-shuffle respectively. To match the convolution operation, we utilized a permute operation to rearrange the original feature map. Based on the above, the modeling process of Conv-Branch can be defined as follows:

$$\begin{aligned} \bar{x}_1 &\in R^{\frac{C}{2} \times H \times W} \leftarrow \text{permute}(x_1) \\ x_1' &= \text{BatchNorm}_1(\bar{x}_1) \\ x_1'' &= \text{ReLU}(\text{BatchNorm}_2(\text{Conv}_{3 \times 3}(x_1'))) \\ x_1''' &= \text{ReLU}(\text{BatchNorm}_3(\text{Conv}_{3 \times 3}(x_1''))) \\ \widehat{x}_1 &= \text{ReLU}(\text{PWConv}(x_1''')) \\ \widetilde{x}_1 &\in R^{H \times W \times \frac{C}{2}} \leftarrow \text{permute}(\widehat{x}_1) \end{aligned}$$

Meanwhile, the modeling process of SSM-Branch can be defined as follows:

$$\begin{aligned} \bar{x}_2 &= \text{LayerNorm}_1(x_2) \\ x_2' &= \text{SiLU}(\text{DWConv}(\text{Linear}(\bar{x}_2))) \\ x_2'' &= \text{LayerNorm}_2(\text{SS2D}(x_2')) \\ x_2''' &= \text{SiLU}(\text{Linear}(\bar{x}_2)) \\ \widetilde{x}_2 &= \text{Linear}(x_2'' \otimes x_2''') \end{aligned}$$

In summary, the output of SS-Conv-SSM be formulated as follows:

$$y = x \oplus g(f^{-1}(\widetilde{x}_1, \widetilde{x}_2))$$

4 Experiments and results

4.1 Datasets

We adopted 16 medical image datasets (As shown in Figure 3), including two private datasets built by ourselves and 14 publicly available datasets to comprehensively evaluate the effectiveness and potential of MedMamba in medical image classification.

PAD-UFES-20 [91]. The PAD-UFES-20 is collected using different smartphone devices. The dataset consists of 2,298 samples of six different types of skin lesions. The skin lesions are: Basal Cell Carcinoma (BCC), Squamous Cell Carcinoma (SCC), Actinic Keratosis (ACK), Seborrheic Keratosis (SEK), Bowen’s disease (BOD), Melanoma (MEL), and Nevus (NEV).

Cervical-US. Cervical-US is a private ultrasound dataset built by ourselves, containing 3,392 Cervical lymph node lesion ultrasound images. Specifically, these images were obtained from 480 patients in the Ultrasound Department of the Second Affiliated Hospital of Guangzhou Medical University. The entire dataset is divided into four categories by clinical experts based on pathological biopsy results: normal lymph nodes (1,217 images), benign lymph nodes (607 images), malignant primary lymph nodes (236 images), and malignant metastatic lymph nodes (1,338 images). The institutional review board approved the use of the dataset.

Fetal-Planes-DB [92]. A large dataset of routinely acquired maternal-fetal screening ultrasound images collected from two different hospitals by several operators and ultrasound machines. All images were manually labeled by an expert maternal fetal clinician. Images are divided into 6 classes: four of the most widely used fetal anatomical planes (Abdomen, Brain, Femur and Thorax), the mother’s cervix (widely used for prematurity screening) and a general category to include any other less common image plane. Fetal brain images are further categorized into the 3 most common fetal brain planes (Trans-thalamic, Trans-cerebellum, Trans-ventricular) to judge fine grain categorization performance.

CPN X-ray [93, 94]. CPN X-ray is a publicly available dataset containing 5,228 chest x-ray images. It helps the researcher and medical community to detect and classify COVID19 and Pneumonia from Chest X-Ray Images using Deep Learning. The entire dataset is divided into three categories: COVID-19, NORMAL, pneumonia.

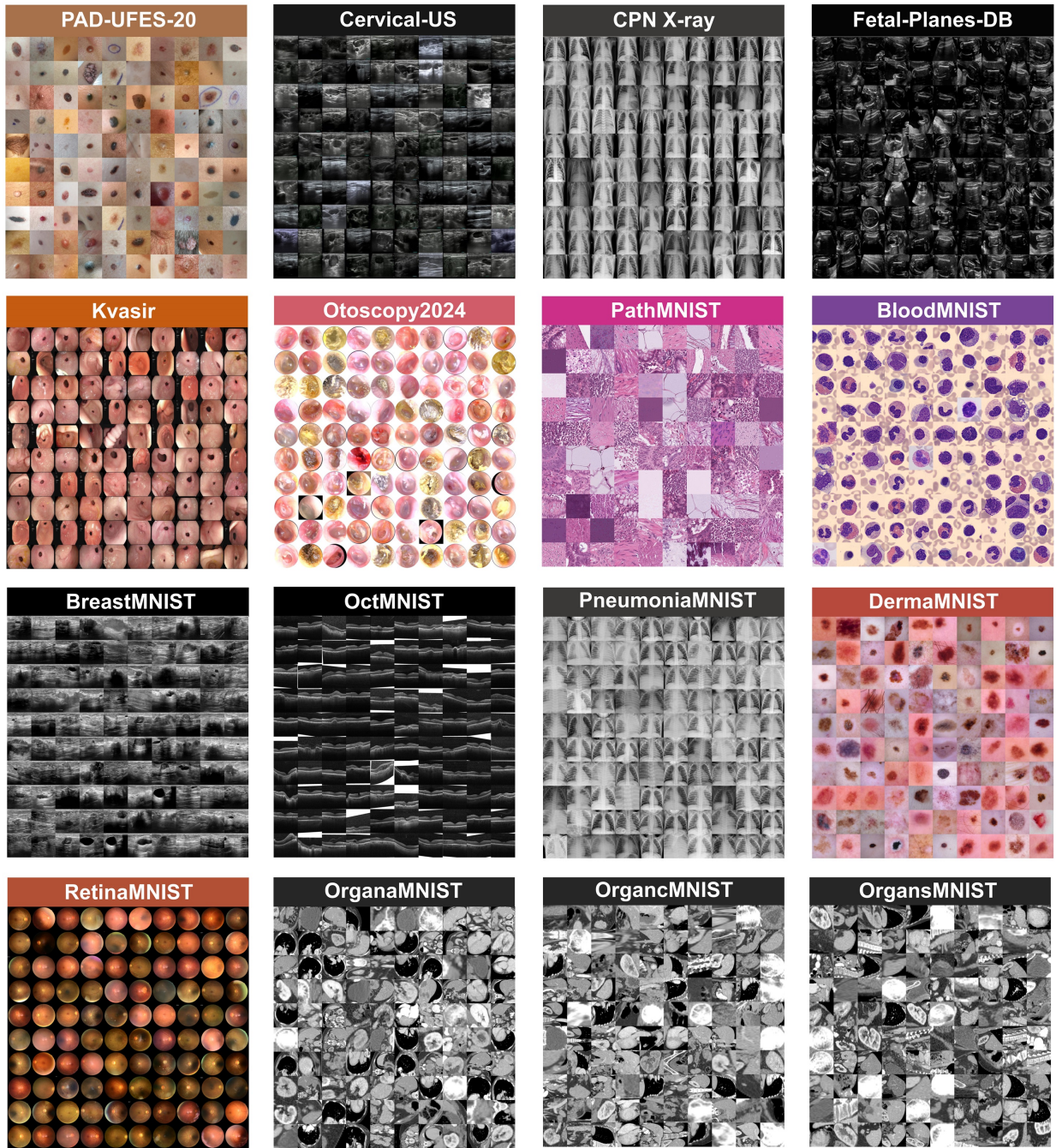


Figure 3: Typical samples of 16 different datasets with different imaging modalities.

Kvasir [95]. The Kvasir dataset consists of images, annotated and verified by medical doctors (experienced endoscopists), including several classes showing anatomical landmarks, pathological findings or endoscopic procedures in the GI tract, i.e., hundreds of images for each class. The anatomical landmarks include Z-line, pylorus, cecum, etc., while the pathological finding includes esophagitis, polyps, ulcerative colitis, etc. In addition, Kvasir provides several sets of images related to removal of lesions, e.g., "dyed and lifted polyp", the "dyed resection margins", etc.

Otoscopy2024 [96]. Otoscopy2024 is a supplement to previous work. In previous work, we collected 20542 endoscopic images of ear infections. On this basis, we have added 2039 images from another medical institution. We name the new dataset as Otoscopy2024. Otoscopy2024 is a large dataset for ear disease classification, consisting of nine categories: Cholesteatoma of middle ear(548 images), Chronic suppurative otitis media(4,021 images), External auditory canal bleeding (451 images), Impacted cerumen (6,058 images), Normal eardrum (4,685 images), Otomycosis externa (2,507 images), Secretory otitis media (2,720 images), Tympanic membrane calcification (1,152 images), Acute otitis media (439 images).

MedMNIST [97, 98]. MedMNIST is a large-scale MNIST-like collection of standardized biomedical images, including 12 datasets for 2D and six datasets for 3D. All images have the corresponding classification labels, so that no background knowledge is required for users. The image size of this dataset includes the following sizes: 28x28 (2D), 64x64 (2D), 128x128 (2D), 224x224 (2D), 28x28x28 (3D) and 64x64x64 (3D). Covering primary data modalities in biomedical images, MedMNIST is designed to perform classification on lightweight 2D and 3D images with various data scales (from 100 to 100,000) and diverse tasks (binary/multi-class, ordinal regression and multi-label). Since MedMNIST is designed to be educational, standardized, diverse and lightweight, it could be used as a general classification benchmark in medical image analysis. In this work, we selected ten 2D medical image classification datasets: PathMNIST, DermaMNIST, OCTMNIST, PneumoniaMNIST, RetinaMNIST, BreastMNIST, BloodMNIST, OrganAMNIST, OrganCMNIST, and OrganSMNIST.

Table 2 reports detailed information of each dataset, such as dataset size, image modality, and dataset splitting strategy. Here, the splitting strategy of MedMNIST is consistent with previous work[15, 98].

Table 2: The detailed descriptions for 16 datasets used in the work.

Name	Imaging Modality	Task (Classes)	Dataset Size	Training/Validation/Test	Data Availability
PAD-UFES-20	Human Skin Smartphone Image	MC (6)	2,298	1,384 / 227 / 687	Public
cervical-US	Cervical lymph Ultrasound	MC (4)	3392	2,039 / 337 / 1,016	Private
CPN X-ray	Chet X-ray	MC (3)	5,228	3,140 / 521 / 1,567	Public
Fetal-Planes-DB	Maternal-fetal Ultrasound	MC (6)	1,2400	7,446 / 1,237 / 3,717	Public
Kvasir	Gastrointestinal Endoscope	MC (8)	4,000	2,408 / 392 / 1,200	Public
Otoscopy2024	Ear Endoscope	MC (9)	24,233	1,4548 / 2,419 / 7,266	Private
PathMNIST	Colon Pathology	MC (9)	107,180	89,996 / 10,004 / 7,180	Public
OCTMNIST	Retinal OCT	MC (4)	109,309	97,477 / 10,832 / 1,000	Public
DermaMNIST	Dermatoscope	MC (7)	10,015	7,007 / 1,003 / 2,005	Public
PneumoniaMNIST	Chest X-Ray	BC (2)	5,856	4,708 / 524 / 624	Public
BreastMNIST	Breast Ultrasound	BC (2)	780	546 / 78 / 156	Public
RetinaMNIST	Fundus Camera	MC (5)	1,600	1,080 / 120 / 400	Public
BloodMNIST	Blood Cell Microscope	MC (8)	17,092	11,959 / 1,712 / 3,421	Public
OrganAMNIST	Abdominal CT	MC (11)	58,850	34,581 / 6,491 / 17,778	Public
OrganCMNIST	Abdominal CT	MC (11)	23,660	13,000 / 2,392 / 8,268	Public
OrganSMNIST	Abdominal CT	MC (11)	25,221	13,940 / 2,452 / 8,829	Public

4.2 Implementation Details

We chose numerous well-designed generic vision networks that perform well on ImageNet to demonstrate the effectiveness and competitiveness of MedMamba in medical image classification. For a fair comparison, we resized all images to 224x224x3 before training each network. Subsequently, each dataset was normalized and standardized.

During the training process of non-MedMNIST (the dataset that does not belong to MedMNIST), we employed the AdamW [99] optimizer with a 0.0001 initial learning rate, B1 of 0.9, B2 of 0.999, and weight decay of 1e-4 and Cross-Entropy Loss to optimize the model parameters. To train the network, we utilized the PyTorch framework. We trained each model for 150 epochs and used a batch size of 64. We used an early-stop strategy to prevent model overfitting. Besides, we did not apply any data augmentation strategy and pre-training to demonstrate as much as possible that the results of all model metrics benefit from MedMamba’s unique architecture.

During the training process of MedMNIST, we followed the same training settings of MedMNISTv2 [97] and MedViT [15] without making any modifications to the original settings. Concretely, we trained all of the MedViT variants (MedMamba-T, MedMamba-S, and MedMamba-B) for 100 epochs and used a batch size of 128. We employed an

AdamW optimizer with an initial learning rate of 0.001, the learning rate is decayed by a factor set of 0.1 in 50 and 75 epochs. In particular, to explore the impact of data augmentation strategies on the performance of MedMamba, we trained MedMamba-T exclusively using the Autoaugment [100] strategy and denoted this new model as MedMamba-X. We then compared all MedMamba models with baseline methods and state-of-the-art methods on MedMNIST. All training processes were conducted on a computer with Ubuntu 22.04 operating system and four NVIDIA GeForce RTX 4090 GPUs.

4.3 Evaluation Metrics

We report Overall Accuracy, Precision, Sensitivity, Specificity, F1-score, and Area under the ROC Curve (AUC) as the standard evaluation metrics. **Overall Accuracy (OA)**: The proportion of all correct predictions (both true positives and true negatives) out of the total number of predictions. **Precision**: The proportion of true positive predictions out of all positive predictions made by the model. **Sensitivity**: The proportion of true positive predictions made by the model out of all actual positive cases. **Specificity**: The proportion of true negative predictions out of all actual negative cases. **F1-score**: The harmonic mean of Precision and Sensitivity, balancing the contributions between two metrics. **AUC**: A metric that quantifies the overall performance of a binary classifier by measuring the area under the Receiver Operating Characteristic (ROC) curve, which plots the true positive rate against the false positive rate at various threshold settings. A higher AUC indicates better model performance in distinguishing between the positive and negative classes.

The calculation formulas for Overall Accuracy, Precision, Sensitivity, Specificity, and F1-score are as follows:

$$\text{Overall Accuracy} = \frac{TP + TN}{TP + TN + FP + FN} \quad (14)$$

$$\text{Precision} = \frac{TP}{TP + FP} \quad (15)$$

$$\text{Sensitivity} = \frac{TP}{TP + FN} \quad (16)$$

$$\text{Specificity} = \frac{TN}{TN + FP} \quad (17)$$

$$\text{F1-score} = \frac{2 * \text{Precision} * \text{Sensitivity}}{\text{Precision} + \text{Sensitivity}} \quad (18)$$

In addition, we also analyzed the model computation complexity (FLOPs) and the model parameter size.

5 Results and discussions

5.1 The performance of MedMamba

We divided reference models for non-MedMNIST into two categories: baseline models and non-baseline models. In this work, baseline models refer to models that have excellent performance in their respective architectures and are widely applied to downstream tasks. ConvNeXt, Swin Transformer (short for Swin) and VMamba were selected as baseline models. Non-baseline models refer to the latest state-of-the-art models (ViTs, CNNs and hybrid networks) with similar parameter sizes to MedMamba.

Table 3 reports the metric results of MedMamba-T and reference models on PAD-UFES-20 and Cervical-US. On PAD-UFES-20, MedMamba-T with the lowest FLOPs achieves 58.8% OA and 0.808 AUC. This result is extremely competitive among reference models. Compared with ConvNeXt-T, MedMamba-T has increased OA and AUC by 4.5% and 0.048 respectively, while significantly reducing model complexity and parameter size. Notably, the AUC and OA of MedMamba-T surpass all non-baseline models. On the Cervical-US dataset, the performance of MedMamba-T is equally impressive. Compared with VMamba-T, Swin-T, and ConvNeXt-T, MedMamba-T achieves the best OA and presents an increase in OA by 1.8%, 6.8%, and 4.0%, respectively. In terms of AUC, MedMamba’s overall performance has surpassed all reference models except for VMamba-T.

Table 4 reports the performance of MedMamba-S and reference models on CPN X-ray and Kvasir. On CPN X-ray, MedMamba-S with the lowest FLOPs achieves the best OA and AUC among all models. Compared with baseline models, the OA of MedMamba-S increases by 0.5% (VMamba-S), 1.9% (Swin-S) and 1.7% (ConvNeXt-S), respectively, while maintaining the fewest parameters. Similarly, the performance of MedMamba-S is impressive on Kvasir. In terms

Table 3: The performance comparison between MedMamba-t and reference models. Red font represents baseline models. Paras, P, Se, Sp, F1 means Parameter size, Precision, Sensitivity, Specificity and F1-score, respectively.

Dataset	Model	FLOPs(G)	Paras	P(%) \uparrow	Se(%) \uparrow	Sp(%) \uparrow	F1(%) \uparrow	OA(%) \uparrow	AUC \uparrow
PAD-UFES-20	MedMamba-T	2.0	14.5	38.4	36.9	89.9	35.8	58.8	0.808
	VMamba-T[42]	4.4	22.1	53.2	40.6	90.0	41.6	59.3	0.804
	Swin-T[69]	4.5	27.5	38.2	41.1	90.6	39.5	60.5	0.830
	ConvNeXt-T[57]	4.5	27.8	37.2	33.6	88.9	33.7	54.3	0.760
	Repvgg-a1[101]	2.6	12.8	34.7	37.7	89.8	35.9	56.7	0.803
	Mobilevitv2-200[102]	5.6	17.4	33.9	32.9	88.0	32.2	49.9	0.705
	EdgeNext-base[103]	2.9	17.9	35.0	36.4	89.9	34.6	57.6	0.802
	Nest-tiny[104]	5.8	16.7	49.9	45.5	91.3	42.3	63.5	0.805
	Mobileone-s4[105]	3.0	12.9	35.9	32.2	87.9	32.3	49.3	0.702
	Cait-xs36[106]	3.8	17.1	37.1	37.8	90.0	37.0	58.6	0.784
DenseNet169[107]	3.4	12.5	44.5	42.4	90.1	41.5	58.0	0.801	
Cervical-US	MedMamba-T	2.0	14.5	81.2	76.2	94.9	78.0	86.2	0.952
	VMamba-T[42]	4.4	22.1	80.4	74.2	94.3	76.4	84.4	0.953
	Swin-T[69]	4.5	27.5	72.0	64.4	92.2	66.3	79.4	0.890
	ConvNeXt-T[57]	4.5	27.8	74.2	68.8	93.4	70.6	82.2	0.931
	Repvgg-a1[101]	2.6	12.8	75.8	73.6	94.7	74.6	85.1	0.937
	Mobilevitv2-200[102]	5.6	17.4	77.6	67.4	93.8	68.1	83.5	0.904
	EdgeNext-base[103]	2.9	17.9	71.1	69.6	92.6	70.2	79.3	0.905
	Nest-tiny[104]	5.8	16.7	78.2	69.8	93.4	72.3	82.3	0.926
	Mobileone-s4[105]	3.0	12.9	72.9	69.3	93.9	70.3	83.4	0.918
	Cait-xs36[106]	3.8	17.1	61.5	57.4	90.8	58.0	75.5	0.860
DenseNet169[107]	3.4	12.5	77.4	78.8	95.0	78.0	85.3	0.947	

of OA, MedMamba-T outperforms all reference models. Regarding AUC, MedMamba’s result is only 0.1% less than the top ranked Deit-small.

Table 5 reports the performance of MedMamba-B and reference models on Fetal-Planes-DB and Otoscopy2024. When the parameters are of similar size, MedMamba-B outperforms all reference models on both datasets. Specifically, MedMamba-B improves OA by 0.6%, 5.2%, and 5.3% on Fetal-Planes-DB compared with VMamba-B, Swin-B, and ConvNeXt, respectively. Importantly, MedMamba-B reduces parameter size by 28.1M, 39.6M, and 40.5M, respectively, while having the lowest FLOPs, which is crucial for practical applications. Regarding the OA of Otoscopy2024, MedMamba-B outperforms all reference models except VMamba-B. Compared with Swin-B and ConvNeXt-B, Model C improves by 1.8

To more intuitively demonstrate the advantages of MedMamba, we presented the average OA and FLOPs of the MedMamba family and the baseline model on non-MedMNIST in Figure 4a. The experimental results show that the average OA of MedMamba-T, MedMamba-S, and MedMamba-B reach 84.0%, 84.3%, and 83.8%, respectively. Regarding average OA, MedMamba variants improve by 0.8%, 1.5%, and 0.7% compared with the three VMamba variants. Compared with the three Swin variants, MedMamba variants improve by 1.9%, 1.3%, and 1.8%, respectively. Compared with the three ConvNeXt variants, MedMamba variants improve by 3.7%, 4.2%, and 4.0%, respectively. As can be seen from Figure 4a, the closer the model is to the upper left corner of the figure, the better the overall performance of the model. Obviously, MedMamba has achieved a good trade-off between parameter size, FLOPs, and OA.

Table 6 reports the performance comparison of MedMamba with previous state-of-the-art methods in terms of the AUC and ACC on each dataset of MedMNIST. Compared with the well-known ResNet18 and ResNet50, the three variants of MedMamba significantly improve the OA and AUC on each dataset. Taking PathMNIST as an example, the OA and AUC of MedMamba-S are 7.2% and 1.0% higher than ResNet50, respectively. Compared with the recent MedViT-S,

Table 4: The performance comparison between MedMamba-S and reference models. Red font represents baseline models. Paras, P, Se, Sp, F1 means Parameter size, Precision, Sensitivity, Specificity and F1-score, respectively.

Dataset	Model	FLOPs(G)	Paras	P(%) \uparrow	Se(%) \uparrow	Sp(%) \uparrow	F1(%) \uparrow	OA(%) \uparrow	AUC \uparrow
CPN X-ray	MedMamba-S	3.5	22.8	97.4	97.4	98.6	97.4	97.3	0.997
	VMamba-S [42]	9.0	43.7	96.8	96.8	98.3	96.8	96.8	0.996
	Swin-S [69]	8.7	48.8	95.4	95.5	97.7	95.4	95.4	0.993
	ConvNext-S [57]	8.7	49.4	95.7	95.7	97.8	95.7	95.6	0.994
	Convformer-s18[108]	4.0	24.7	95.9	95.8	97.8	95.8	95.7	0.992
	TNT-s[109]	5.2	23.3	93.4	93.4	96.6	93.4	93.2	0.987
	Caformer-s18[108]	4.1	24.3	95.5	95.5	97.7	95.5	95.4	0.992
	PvtV2-b2[110]	4.0	24.8	96.3	96.2	98.1	96.2	96.2	0.994
	Davit-tiny [111]	4.5	27.6	95.1	95.2	97.5	95.1	95.1	0.993
	Deit-small[112]	4.6	21.7	95.2	95.1	97.5	95.1	95.1	0.990
	EfficientNetV2-s[113]	8.3	20.2	95.8	95.7	97.8	95.7	95.7	0.993
	Coat-small[114]	12.6	21.4	94.3	94.2	97.0	94.2	94.1	0.987
Kvasir	MedMamba-T	3.5	22.8	79.4	79.3	97.0	79.2	79.3	0.976
	VMamba-S [42]	9.0	43.7	77.6	77.3	96.8	77.1	77.3	0.970
	Swin-S [69]	8.7	48.8	78.4	78.0	96.9	77.3	78.0	0.973
	ConvNext-S [57]	8.7	49.4	75.6	74.8	96.1	74.8	74.8	0.969
	Convformer-s18[108]	4.0	24.7	76.4	75.8	96.5	75.6	75.8	0.970
	TNT-s[109]	5.2	23.3	76.5	76.2	96.6	75.7	76.2	0.953
	Caformer-s18[108]	4.1	24.3	73.6	73.7	96.2	73.5	73.7	0.960
	PvtV2-b2[110]	4.0	24.8	75.7	75.6	96.5	75.3	75.6	0.958
	Davit-tiny[111]	4.5	27.6	73.8	73.6	96.2	73.0	73.6	0.966
	Deit-small[112]	4.6	21.7	78.2	78.1	96.8	77.9	78.1	0.977
	EfficientNetV2-s[113]	8.3	20.2	78.7	78.1	96.8	78.1	78.2	0.972
	Coat-small[114]	12.6	21.4	74.2	73.5	96.2	73.1	73.5	0.969

the OA and AUC of MedMamba-S on OCTMNIST increase by 14.7% and 3.6%, respectively, which indicates that MedMamba may have a clear advantage in the OCT image-based classification tasks. Overall, our MedMamba effectively improves the performance of medical image classification tasks in the MedMNIST benchmark, especially PathMNIST, OCTMNIST, BloodMNIST, OrganaMNIST and OrgansMNIST. To more intuitively demonstrate the potential of MedMamba on MedMNIST, we presented each model’s average OA and FLOPs in Figure 4b. Experimental results show that the average OA of MedMamba-T, MedMamba-S, and MedMamba-B reaches 86.2%, 87.0% and 87.4% respectively. Compared with MedViT-T, MedViT-S, and MedViT-L, our MedMamba improves by 2.0%, 1.7% and 2.9%, respectively. In particular, the FLOPs and parameter size of the MedMamba family are significantly lower than those of the MedViT family, which is helpful for practical applications and subsequent model improvements. As can be seen from Figure 4b, the closer the model is to the upper left corner of the figure, the better the overall performance of the model. Obviously, MedMamba has achieved a good trade-off between parameter size, FLOPs, and OA for MedMNIST. In summary, MedMamba performs well on most medical image classification tasks on MedMNIST, establishing a new baseline and achieving state-of-the-art results. Moreover, as shown in Table 6 and Figure 4, when data augmentation is used, the average OA of MedMamba-X significantly surpasses the original MedMamba-T. Therefore, we recommend that future work adopt AutoAugment during model training.

5.2 Visual Interpretation for MedMamba

In order to enhance the transparency of MedMamba and enhance user trust in the model, we adopted Grad-CAM [125] to visualize and examine MedMamba’s internal decision-making mechanism. The Grad-CAM is presented with a

Table 5: The performance comparison between MedMamba-B and reference models. Red font represents baseline models. Paras, P, Se, Sp, F1 means Parameter size, Precision, Sensitivity, Specificity and F1-score, respectively.

Dataset	Model	FLOPs(G)	Paras	P(%) \uparrow	Se(%) \uparrow	Sp(%) \uparrow	F1(%) \uparrow	OA(%) \uparrow	AUC \uparrow
Fetal-Planes-DB	MedMamba-B	7.4	47.1	92.8	93.8	98.8	93.3	94.4	0.993
	VMamba-B [42]	15.1	75.2	92.2	93.4	98.7	92.7	93.8	0.994
	Swin-B [69]	15.4	86.7	86.1	84.9	97.7	85.4	89.2	0.982
	ConvNext-B [57]	15.4	87.6	85.9	85.2	97.7	85.5	89.1	0.982
	Davit-small[111]	8.8	48.9	85.9	84.8	97.6	85.3	88.9	0.977
	Mvitv2-base[115]	10.0	50.7	89.9	90.1	98.3	89.9	91.9	0.989
	EfficientNet-b6[116]	19.0	40.8	91.2	91.2	98.4	91.1	92.8	0.993
	EfficientNetV2-b[113]	24.5	52.9	87.6	89.1	97.9	88.3	90.2	0.983
	FocalNet-s[117]	8.7	49.1	91.7	90.9	98.5	91.2	92.9	0.989
	Twins-SVT-base[118]	8.8	48.9	87.5	88.4	97.9	88.0	90.3	0.987
	Poolformer-m36[119]	8.8	55.4	82.7	82.3	87.4	82.9	87.67	0.973
	Xcit-s[120]	9.1	47.3	85.2	86.1	97.7	85.5	89.1	0.981
GcVit-s[121]	8.4	50.3	84.5	84.3	97.5	84.3	88.4	0.977	
Otoscopy2024	MedMamba-B	7.4	47.1	87.7	83.7	98.7	85.4	89.9	0.988
	VMamba-B [42]	15.1	75.2	86.7	92.9	98.6	84.6	90.1	0.988
	Swin-B [69]	15.4	86.7	83.1	80.8	98.4	81.7	88.1	0.987
	ConvNext-B [57]	15.4	87.6	80.2	75.8	98.1	77.6	85.2	0.980
	Davit-small[111]	8.8	48.9	77.9	73.5	97.8	75.4	83.3	0.971
	Mvitv2-base[115]	10.0	50.7	83.5	90.7	98.4	81.8	88.1	0.981
	EfficientNet-b6[116]	19.0	40.8	84.0	81.4	98.5	82.5	88.7	0.989
	EfficientNetV2-b[113]	24.5	52.9	81.9	78.5	98.2	79.8	86.3	0.981
	FocalNet-s[117]	8.7	49.1	82.9	82.5	98.4	82.6	87.9	0.982
	Twins-SVT-base[118]	8.8	48.9	82.8	78.3	98.2	80.3	86.6	0.979
	Poolformer-m36[119]	8.8	55.4	79.1	73.0	97.9	75.4	84.0	0.969
	Xcit-s[120]	9.1	47.3	82.5	80.3	98.4	81.4	87.5	0.982
GcVit-s[121]	8.4	50.3	84.5	78.8	98.3	81.1	87.5	0.983	

rainbow colormap scale, where the red color stands for high relevance, yellow stands for medium relevance, and blue stands for low relevance. In Figure 5, we presented the heatmap results of MedMamba-S for typical images in each dataset. It is obvious that in most cases, our model can accurately focus on the lesion areas in each type of image, and rarely pay attention to the background parts that are not related to the prediction results.

The t-SNE (t-distributed Stochastic Neighbor Embedding) is an unsupervised non-linear dimensionality reduction technique for data exploration and visualizing high-dimensional data. It is often used to visualize complex datasets into two and three dimensions, allowing researchers to understand more about underlying patterns and relationships in the data. We plotted the t-SNE results of MedMamba-S, Swin-S, ConvNeXt-S in Figure 6. The experimental results show that compared with the baseline models Swin-S and ConvNeXt-S, the features extracted by MedMamba are obviously more representative and discriminative. Specifically, in the t-SNE two-dimensional feature space constructed by MedMamba, sample points of the same category exhibit a significant clustering phenomenon, while sample points of different categories are relatively dispersed, reflecting MedMamba’s effectiveness in capturing differences between categories. On the contrary, the baseline models Swin-S and ConvNeXt-S perform poorly in distinguishing samples from different categories, failing to effectively highlight the differences between categories, resulting in a more chaotic sample distribution. The above results indicate that MedMamba has better modeling ability for medical images.

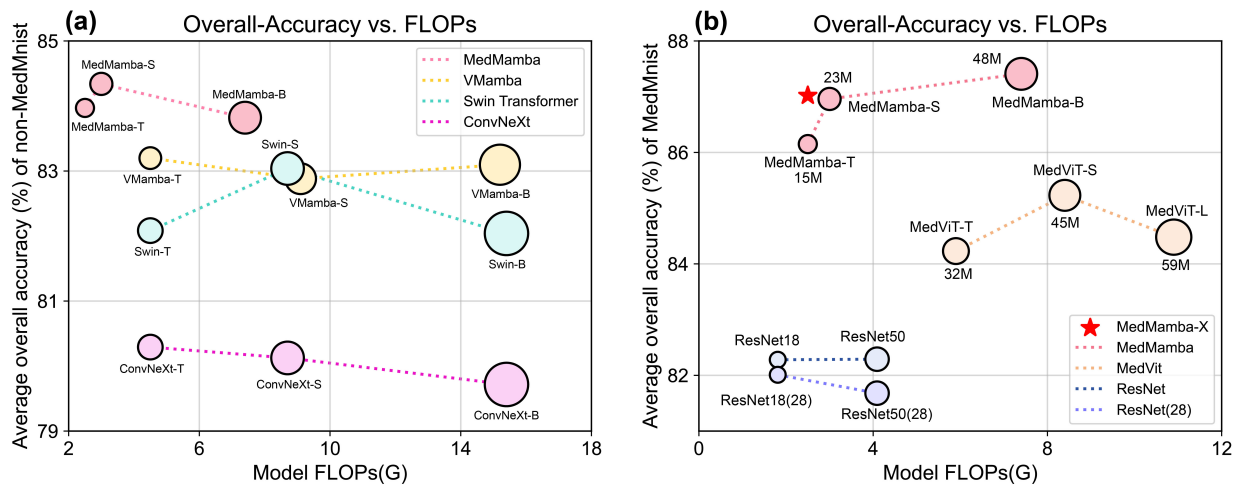


Figure 4: The performance comparison between MedMamba and reference models (Larger circles mean more parameters). a: The performance of MedMamba and baseline reference models on non-MedMNIST. b: The performance of MedMamba, MedViT and ResNet on MedMNIST.

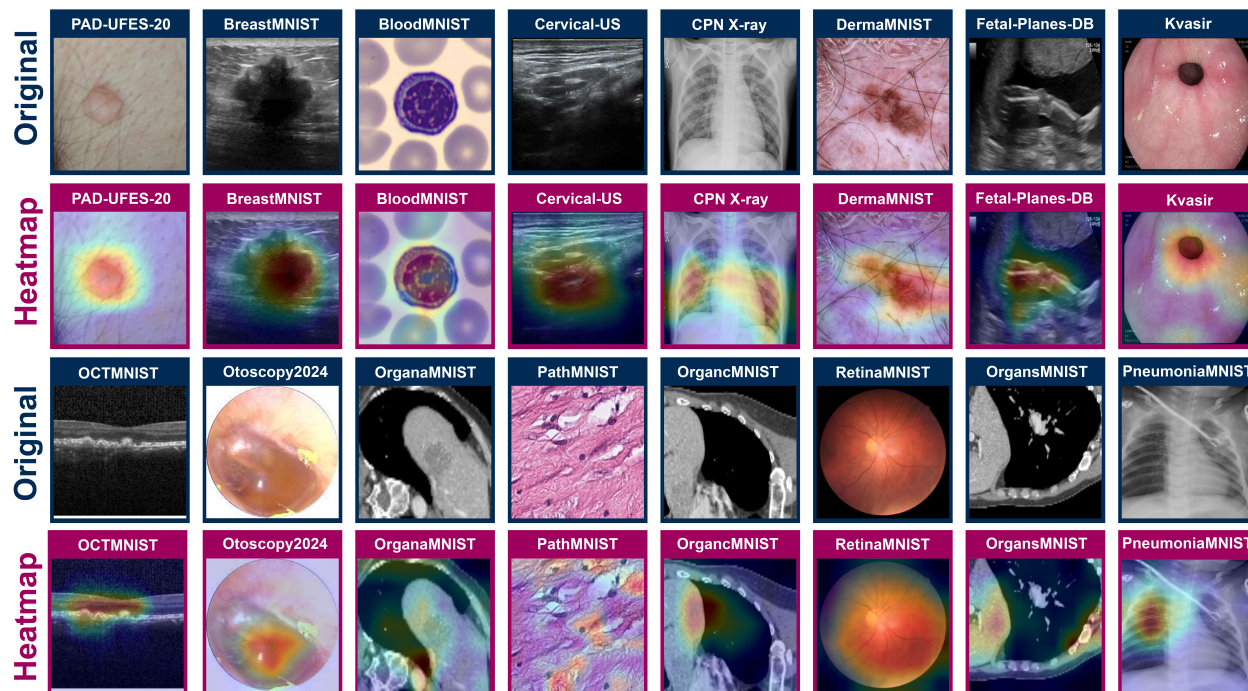


Figure 5: The visual heatmaps of MedMamba-S using Grad-CAM on 16 datasets.

Table 6: The performance of MedMamba-T on various datasets and comparison with reference models. (**Bold font** represents the best value. AOA represents the average overall accuracy of the model.)

Methods	PathMNIST		DermaMNIST		OCTMNIST		PneumoniaMNIST		RetinaMNIST	
	AUC	OA	AUC	OA	AUC	OA	AUC	OA	AUC	OA
ResNet18 (28)[53]	0.983	0.907	0.917	0.735	0.943	0.743	0.944	0.854	0.717	0.524
ResNet18 (224)[53]	0.989	0.909	0.920	0.754	0.958	0.763	0.956	0.864	0.710	0.493
ResNet50 (28) [53]	0.990	0.911	0.913	0.735	0.952	0.762	0.948	0.854	0.726	0.528
ResNet50 (224)[53]	0.989	0.892	0.912	0.731	0.958	0.776	0.962	0.884	0.716	0.511
Auto-sklearn[122]	0.934	0.716	0.902	0.719	0.887	0.601	0.942	0.855	0.690	0.515
AutoKeras [123]	0.959	0.834	0.915	0.749	0.955	0.763	0.947	0.878	0.719	0.503
Google AutoML[124]	0.944	0.728	0.914	0.768	0.963	0.771	0.991	0.946	0.750	0.531
MedVit-T [15]	0.994	0.938	0.914	0.768	0.961	0.767	0.993	0.949	0.752	0.534
MedVit-S [15]	0.993	0.942	0.937	0.780	0.960	0.782	0.995	0.961	0.773	0.561
MedVit-L [15]	0.984	0.933	0.920	0.773	0.945	0.761	0.991	0.921	0.754	0.552
MedMamba-T	0.997	0.953	0.917	0.779	0.992	0.918	0.965	0.899	0.747	0.543
MedMamba-S	0.997	0.955	0.924	0.758	0.991	0.929	0.976	0.936	0.718	0.545
MedMamba-B	0.999	0.964	0.925	0.757	0.996	0.927	0.973	0.925	0.715	0.553
MedMamba-X	0.999	0.962	0.918	0.751	0.993	0.928	0.964	0.910	0.719	0.570

Methods	BreastMNIST		BloodMNIST		OrganAMNIST		OrganCMNIST		OrganSMNIST	
	AUC	OA	AUC	OA	AUC	OA	AUC	OA	AUC	OA
ResNet18 (28) [53]	0.901	0.863	0.998	0.958	0.997	0.935	0.992	0.900	0.972	0.782
ResNet18 (224)[53]	0.891	0.833	0.998	0.963	0.998	0.951	0.94	0.920	0.974	0.778
ResNet50 (28) [53]	0.857	0.812	0.997	0.956	0.997	0.935	0.992	0.905	0.972	0.770
ResNet50 (224) [53]	0.866	0.842	0.997	0.950	0.998	0.947	0.993	0.911	0.975	0.785
Auto-sklearn [122]	0.836	0.803	0.987	0.878	0.963	0.762	0.976	0.829	0.945	0.672
AutoKeras [123]	0.871	0.831	0.998	0.961	0.994	0.905	0.990	0.879	0.974	0.813
Google AutoML[124]	0.919	0.861	0.998	0.966	0.990	0.886	0.988	0.877	0.964	0.749
MedVit-T[15]	0.934	0.896	0.996	0.950	0.995	0.931	0.991	0.901	0.972	0.789
MedVit-S[15]	0.938	0.897	0.997	0.951	0.996	0.928	0.993	0.916	0.987	0.805
MedVit-L[15]	0.929	0.883	0.996	0.954	0.997	0.943	0.994	0.922	0.973	0.806
MedMamba-T	0.825	0.853	0.999	0.978	0.998	0.946	0.997	0.927	0.982	0.819
MedMamba-S	0.806	0.853	0.999	0.984	0.999	0.959	0.997	0.944	0.984	0.833
MedMamba-B	0.849	0.891	0.999	0.983	0.999	0.964	0.997	0.943	0.984	0.834
MedMamba-X	0.898	0.853	0.999	0.984	0.999	0.967	0.998	0.947	0.983	0.830

5.3 Robustness Analysis

To facilitate the practical application and subsequent improvement of MedMamba, we referred to related work practices [126, 127, 128] to analyze its robustness. Concretely, we artificially corrupted the original dataset to simulate various interferences that the model may encounter in practical clinical settings and observed the performance changes of the model under different perturbations. By testing MedMamba-X (As shown in Figure 7) on the Otoscopy2024, BloodMNIST, Fetal-Planes-DB, and DermMNIST datasets, we found the following phenomena: When corrupting the Otoscopy2024 dataset, MedMamba-X is particularly sensitive to the perturbation of image rotation, as shown by the downward trend in the results of all evaluation metrics. In contrast, for the BloodMNIST dataset, the color temperature change has the most significant impact on the performance of MedMamba-X. In particular, in terms of OA, the model’s performance has decreased from 98.4% to 95.1%. On the Fetal-Planes-DB dataset, image translation has a more obvious impact on the performance of the model. Regarding the OA, the model’s results decreased by 3.4%. Similar to the findings on BloodMNIST, when perturbations based on color temperature changes are introduced, the

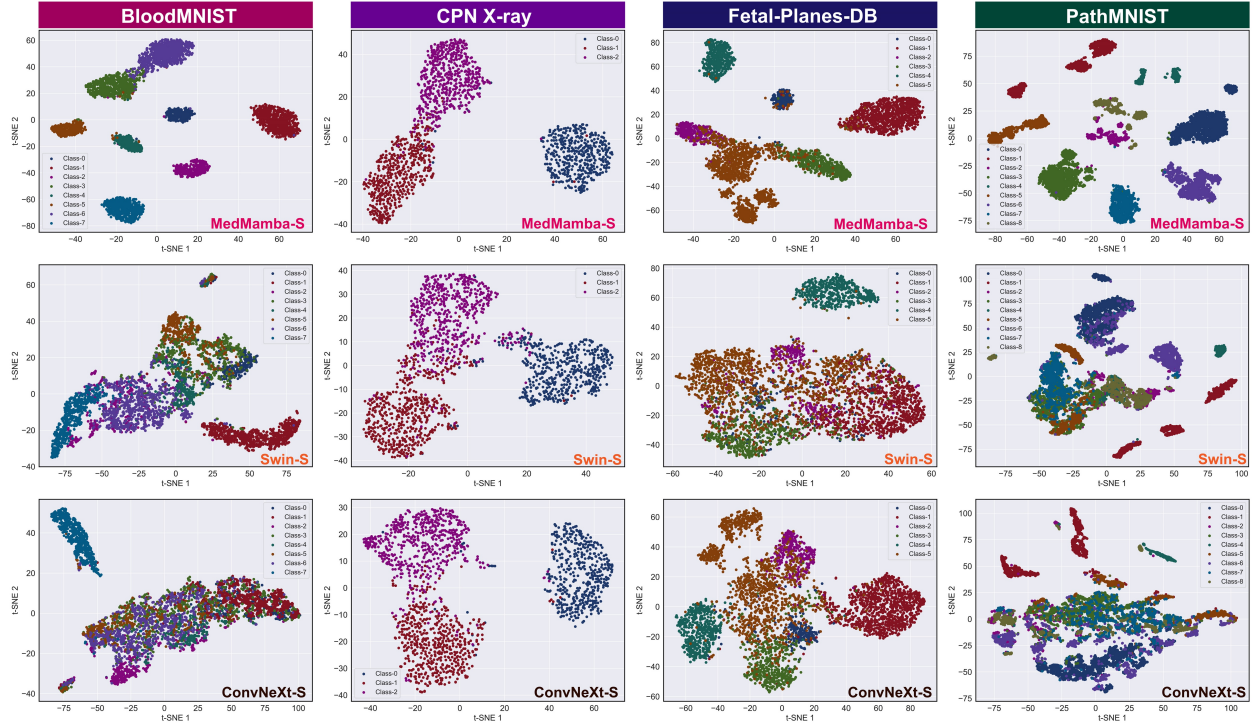


Figure 6: The t-SNE results of MedMamba-S and baseline models for CPN X-ray, Fetal-Planes-DB, BloodMNIST and PathMNIST.

performance of the model on all evaluation metrics decline. Overall, however, MedMamba maintains relatively stable performance in most cases of image perturbation.

5.4 Ablation Study

We conducted various ablation experiments to investigate the effectiveness of the critical components of our architecture. Table 7 reports in detail the performance changes of MedMamba-X with different components. Specifically, when only SSM is used (denoted as Base Model-I), all metric results of the model are at the lowest level. Notably, when we integrated the Conv-branch on its basis (denoted as Base Model-II) and directly used element-wise addition to fuse the results of the SSM-branch and the Conv-branch, the model’s performance was significantly improved. Taking PathMNIST and Otoscopy2024 as examples, the OA of Base Model-II is improved by 1.5% and 1.3%, respectively compared with Base Model-I. Unfortunately, this simple strategy will lead to a sharp increase in model complexity and parameter size, i.e., the parameter size and FLOPs of the model increased by 35.4M and 5.4G, respectively. This problem has been effectively alleviated by introducing the idea of grouped convolution, i.e., the channel-split operation. Furthermore, the channel-shuffle operation further strengthens the interaction of channel information between different groups and improves the performance of the model without increasing FLOPs and parameter size. Such improvements demonstrate that while optimizing model performance, we have also effectively controlled the complexity and parameter size of the model, achieving a balance between performance and efficiency.

6 Conclusion

In summary, we proposed the MedMamba family in this work, which is the first vision mamba for general medical image classification. Although customized architectures designed for specific medical image datasets are superior in accuracy and efficiency, our MedMamba is able to extract local feature representations and long-range dependencies for performing generalized medical image classification tasks by combining classic convolutional layers and SSM modules. In particular, by introducing the grouped convolution strategy inside it, MedMamba achieves a good trade-off between efficient modeling and computational resource consumption. Extensive experiments show that our MedMamba achieves extremely competitive performance on 16 datasets containing ten image modalities and 411,007 images compared with

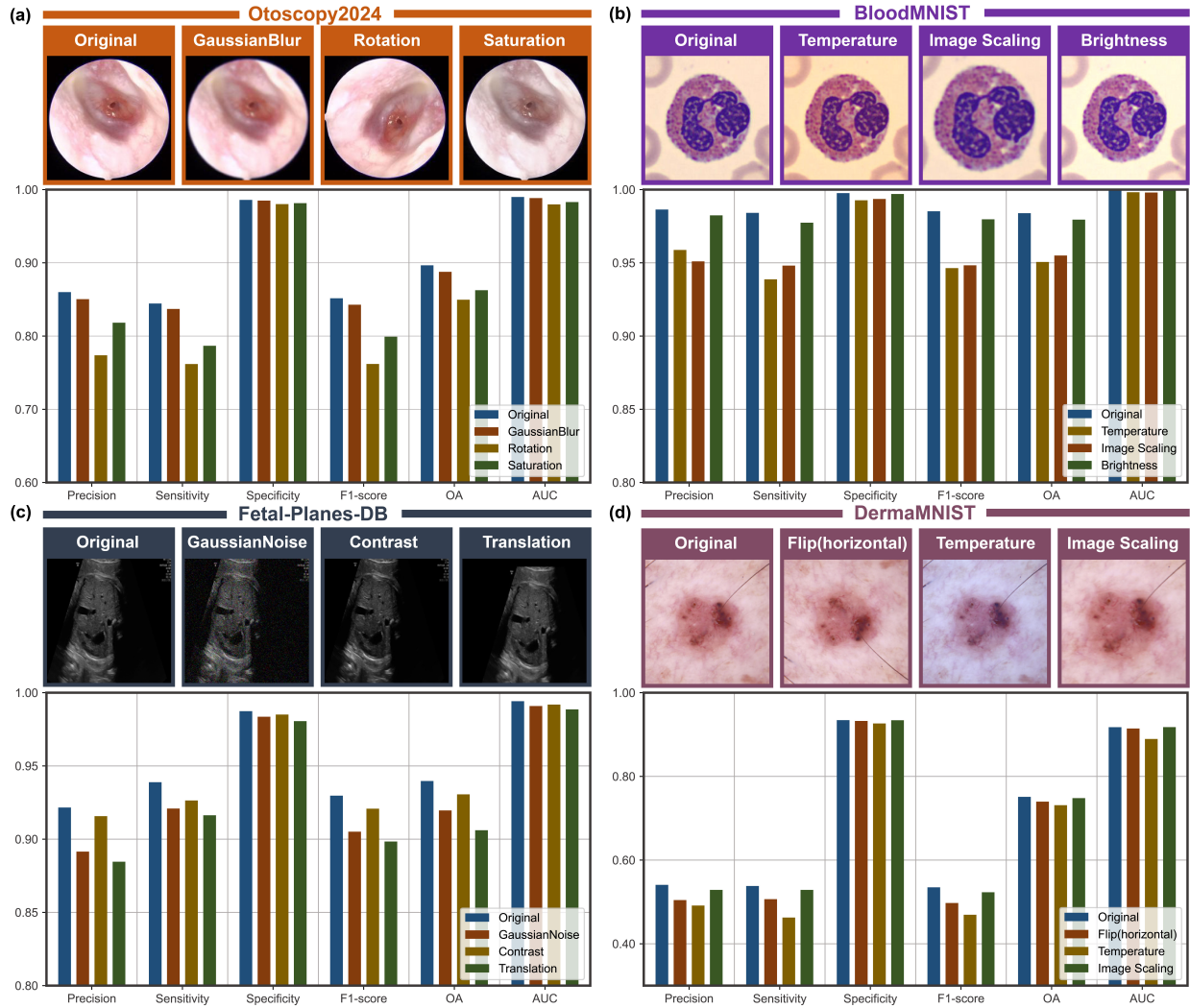


Figure 7: Performance comparison of MedMamba-X under different image perturbations. a: Robustness analysis results of Otoscopy2024. b: Robustness analysis results of BloodMNIST. c: Robustness analysis results of Fetal-Planes-DB. d: Robustness analysis results of DermMNIST.

state-of-the-art methods. We hope that this work can provide inspiration for future work in Mamba-based and model architecture design and intelligent medical applications.

In addition, we summarize our future work into the following points: 1) We will further explore and test the potential of MedMamba on medical datasets obtained from other imaging modalities, and optimize the internal architecture of MedMamba. 2) We will further use explainable artificial intelligence to analyze MedMamba’s decision-making mechanism. In addition, the impact of MedMamba’s inference speed and model parameter size on practical applications should also be studied. 3) Due to the advantages of SSM in modeling long-range dependencies, further research on the performance of MedMamba in some high-resolution medical images (such as pathological images) may be beneficial. 4) We will attempt to use the backbone of MedMamba as an encoder or decoder to explore its application potential in more advanced medical image tasks, such as medical image segmentation, medical object detection, medical image registration, and medical image reconstruction.

Table 7: The performance of MedMamba-T with different components for various datasets. Paras represents parameter size. ‘SP’ and ‘SF’ represents Channel-Split and Channel-Shuffle, respectively.

Dataset	Components				Evaluation metrics			
	SSM	Conv	SP	SF	FLOPs(G)↓	Paras(M)↓	OA(%)↑	AUC↑
Cervical-US	✓	✗	✗	✗	2.0	16.2	83.9	0.939
	✓	✓	✗	✗	7.4	51.6	85.1	0.937
	✓	✓	✓	✗	2.0	14.5	85.4	0.941
	✓	✓	✓	✓	2.0	14.5	85.6	0.953
PathMNIST	✓	✗	✗	✗	2.0	16.2	94.4	0.993
	✓	✓	✗	✗	7.4	51.6	95.9	0.997
	✓	✓	✓	✗	2.0	14.5	95.0	0.994
	✓	✓	✓	✓	2.0	14.5	95.3	0.997
CPN X-ray	✓	✗	✗	✗	2.0	16.2	96.3	0.993
	✓	✓	✗	✗	7.4	51.6	97.4	0.997
	✓	✓	✓	✗	2.0	14.5	96.8	0.995
	✓	✓	✓	✓	2.0	14.5	97.1	0.995
OCTMNIST	✓	✗	✗	✗	2.0	16.2	91.4	0.986
	✓	✓	✗	✗	7.4	51.6	92.3	0.995
	✓	✓	✓	✗	2.0	14.5	91.5	0.993
	✓	✓	✓	✓	2.0	14.5	91.8	0.992
Otoscopy2024	✓	✗	✗	✗	2.0	16.2	88.4	0.983
	✓	✓	✗	✗	7.4	51.6	89.7	0.990
	✓	✓	✓	✗	2.0	14.5	89.1	0.985
	✓	✓	✓	✓	2.0	14.5	89.5	0.989

Data Availability

The codes and pre-trained weights of MedMamba family and access links to public datasets are available at <https://github.com/YubiaoYue/MedMamba>. The Cervical-US and Otoscopy2024 that support the findings of this study are available on request from the corresponding author upon reasonable request.

Acknowledgments

This work is supported NSF of Guangdong Province (No.2022A1515011044 and No. 2023A1515010885), the project of promoting research capabilities for key constructed disciplines in Guangdong Province (No. 2021ZDJS028), Guangzhou Science and Technology Plan Project (No. 202201011696), the scientific research capacity improvement project of the doctoral program construction unit of Guangdong Polytechnic Normal University in 2022 (No. 22GPNUZDJS31). In addition, we would like to express our gratitude to VMamba, VM-UNet, and Swin-UMamba for their open source.

References

- [1] Li Liu, Haocheng Sun, and Fanzhang Li. A lie group kernel learning method for medical image classification. *Pattern Recognition*, 142:109735, 2023.
- [2] Samir S Yadav and Shivajirao M Jadhav. Deep convolutional neural network based medical image classification for disease diagnosis. *Journal of Big data*, 6(1):1–18, 2019.
- [3] Zhongwen Li, Jiwei Jiang, Kuan Chen, Qianqian Chen, Qinxiang Zheng, Xiaotian Liu, Hongfei Weng, Shanjun Wu, and Wei Chen. Preventing corneal blindness caused by keratitis using artificial intelligence. *Nature communications*, 12(1):3738, 2021.
- [4] Danh-Tai Hoang, Eldad D Shulman, Rust Turakulov, Zied Abdullaev, Omkar Singh, Emma M Campagnolo, H Lalchungnunga, Eric A Stone, MacLean P Nasrallah, Eytan Ruppim, et al. Prediction of dna methylation-based tumor types from histopathology in central nervous system tumors with deep learning. *Nature Medicine*, pages 1–10, 2024.
- [5] Xinke Zhang, Zihan Zhao, Ruixuan Wang, Haohua Chen, Xueyi Zheng, Lili Liu, Lilong Lan, Peng Li, Shuyang Wu, Qinghua Cao, et al. A multicenter proof-of-concept study on deep learning-based intraoperative discrimination of primary central nervous system lymphoma. *Nature Communications*, 15(1):3768, 2024.
- [6] Shih-Cheng Huang, Anuj Pareek, Malte Jensen, Matthew P Lungren, Serena Yeung, and Akshay S Chaudhari. Self-supervised learning for medical image classification: a systematic review and implementation guidelines. *NPJ Digital Medicine*, 6(1):74, 2023.

- [7] Eyal Bercovich and Marcia C Javitt. Medical imaging: from roentgen to the digital revolution, and beyond. *Rambam Maimonides medical journal*, 9(4), 2018.
- [8] Zhongyu Li, Xiaofan Zhang, Henning Müller, and Shaoting Zhang. Large-scale retrieval for medical image analytics: A comprehensive review. *Medical image analysis*, 43:66–84, 2018.
- [9] Yun Yang, Yuanyuan Hu, Xingyi Zhang, and Song Wang. Two-stage selective ensemble of cnn via deep tree training for medical image classification. *IEEE Transactions on Cybernetics*, 52(9):9194–9207, 2021.
- [10] Xuxin Chen, Ximin Wang, Ke Zhang, Kar-Ming Fung, Theresa C Thai, Kathleen Moore, Robert S Mannel, Hong Liu, Bin Zheng, and Yuchen Qiu. Recent advances and clinical applications of deep learning in medical image analysis. *Medical Image Analysis*, 79:102444, 2022.
- [11] Hiroshi Fujita. Ai-based computer-aided diagnosis (ai-cad): the latest review to read first. *Radiological physics and technology*, 13(1):6–19, 2020.
- [12] Chan-Woo Park, Sung Wook Seo, Noeul Kang, BeomSeok Ko, Byung Wook Choi, Chang Min Park, Dong Kyung Chang, Hwiuoung Kim, Hyunchul Kim, Hyunna Lee, et al. Artificial intelligence in health care: Current applications and issues. *Journal of Korean medical science*, 35(42), 2020.
- [13] Weibin Wang, Dong Liang, Qingqing Chen, Yutaro Iwamoto, Xian-Hua Han, Qiaowei Zhang, Hongjie Hu, Lanfen Lin, and Yen-Wei Chen. Medical image classification using deep learning. *Deep learning in healthcare: paradigms and applications*, pages 33–51, 2020.
- [14] Rehan Ashraf, Muhammad Asif Habib, Muhammad Akram, Muhammad Ahsan Latif, Muhammad Sheraz Arshad Malik, Muhammad Awais, Saadat Hanif Dar, Toqeer Mahmood, Muhammad Yasir, and Zahoor Abbas. Deep convolution neural network for big data medical image classification. *IEEE Access*, 8:105659–105670, 2020.
- [15] Omid Nejati Manzari, Hamid Ahmadabadi, Hossein Kashiani, Shahriar B Shokouhi, and Ahmad Ayatollahi. Medvit: a robust vision transformer for generalized medical image classification. *Computers in Biology and Medicine*, 157:106791, 2023.
- [16] Junlong Cheng, Shengwei Tian, Long Yu, Chengrui Gao, Xiaojing Kang, Xiang Ma, Weidong Wu, Shijia Liu, and Hongchun Lu. Resganet: Residual group attention network for medical image classification and segmentation. *Medical Image Analysis*, 76:102313, 2022.
- [17] Wenjian Gan, Yang Zhou, Xiaofei Hu, Luying Zhao, Gaoshuang Huang, and Chenglong Zhang. Convolutional mlp orthogonal fusion of multiscale features for visual place recognition. *Scientific Reports*, 14(1):11756, 2024.
- [18] Zewen Li, Fan Liu, Wenjie Yang, Shouheng Peng, and Jun Zhou. A survey of convolutional neural networks: analysis, applications, and prospects. *IEEE transactions on neural networks and learning systems*, 33(12):6999–7019, 2021.
- [19] Kai Han, Yunhe Wang, Hanting Chen, Xinghao Chen, Jianyuan Guo, Zhenhua Liu, Yehui Tang, An Xiao, Chunjing Xu, Yixing Xu, et al. A survey on vision transformer. *IEEE transactions on pattern analysis and machine intelligence*, 45(1):87–110, 2022.
- [20] Jia Deng, Wei Dong, Richard Socher, Li-Jia Li, Kai Li, and Li Fei-Fei. Imagenet: A large-scale hierarchical image database. In *2009 IEEE conference on computer vision and pattern recognition*, pages 248–255. Ieee, 2009.
- [21] Jianpeng Zhang, Yutong Xie, Qi Wu, and Yong Xia. Medical image classification using synergic deep learning. *Medical image analysis*, 54:10–19, 2019.
- [22] Jindong Gu, Volker Tresp, and Yao Qin. Are vision transformers robust to patch perturbations? In *European Conference on Computer Vision*, pages 404–421. Springer, 2022.
- [23] Zhiliang Peng, Zonghao Guo, Wei Huang, Yaowei Wang, Lingxi Xie, Jianbin Jiao, Qi Tian, and Qixiang Ye. Conformer: Local features coupling global representations for recognition and detection. *IEEE Transactions on Pattern Analysis and Machine Intelligence*, 2023.
- [24] Tao Wang, Junlin Lan, Zixin Han, Ziwei Hu, Yuxiu Huang, Yanglin Deng, Hejun Zhang, Jianchao Wang, Musheng Chen, Haiyan Jiang, et al. O-net: a novel framework with deep fusion of cnn and transformer for simultaneous segmentation and classification. *Frontiers in neuroscience*, 16:876065, 2022.
- [25] Xiangzuo Huo, Gang Sun, Shengwei Tian, Yan Wang, Long Yu, Jun Long, Wendong Zhang, and Aolun Li. Hifuse: Hierarchical multi-scale feature fusion network for medical image classification. *Biomedical Signal Processing and Control*, 87:105534, 2024.
- [26] Zhengqi Dong, Benzhu Xu, Jun Shi, and Liping Zheng. Local and global feature interaction network for endoscope image classification. In *International Conference on Image and Graphics*, pages 412–424. Springer, 2023.

- [27] Javad Mirzapour Kaleybar, Hooman Saadat, and Hooman Khaloo. Capturing local and global features in medical images by using ensemble cnn-transformer. In *2023 13th International Conference on Computer and Knowledge Engineering (ICCKE)*, pages 030–035. IEEE, 2023.
- [28] Ming Fang, Minghan Fu, Bo Liao, Xiujuan Lei, and Fang-Xiang Wu. Deep integrated fusion of local and global features for cervical cell classification. *Computers in Biology and Medicine*, page 108153, 2024.
- [29] Zhaoshan Liu and Lei Shen. Cect: Controllable ensemble cnn and transformer for covid-19 image classification. *Computers in Biology and Medicine*, 173:108388, 2024.
- [30] Xin Wu, Yue Feng, Hong Xu, Zhuosheng Lin, Tao Chen, Shengke Li, Shihan Qiu, Qichao Liu, Yuangang Ma, and Shuangsheng Zhang. Ctranscnn: Combining transformer and cnn in multilabel medical image classification. *Knowledge-Based Systems*, 281:111030, 2023.
- [31] Bangkang Fu, Mudan Zhang, Junjie He, Ying Cao, Yuchen Guo, and Rongpin Wang. Stohisnet: A hybrid multi-classification model with cnn and transformer for gastric pathology images. *Computer Methods and Programs in Biomedicine*, 221:106924, 2022.
- [32] Zhentao Hu, Yanyang Li, Zheng Wang, Shuo Zhang, Wei Hou, Alzheimer’s Disease Neuroimaging Initiative, et al. Conv-swinformer: Integration of cnn and shift window attention for alzheimer’s disease classification. *Computers in Biology and Medicine*, 164:107304, 2023.
- [33] Feiniu Yuan, Zhengxiao Zhang, and Zhijun Fang. An effective cnn and transformer complementary network for medical image segmentation. *Pattern Recognition*, 136:109228, 2023.
- [34] Ziheng Wang, Xionguo Min, Fangyu Shi, Ruinian Jin, Saida S Nawrin, Ichen Yu, and Ryoichi Nagatomi. Smeswin unet: Merging cnn and transformer for medical image segmentation. In *International Conference on Medical Image Computing and Computer-Assisted Intervention*, pages 517–526. Springer, 2022.
- [35] Nagur Shareef Shaik, Teja Krishna Cherukuri, N Veeranjaneulu, and Jyostna Devi Bodapati. Medtransnet: advanced gating transformer network for medical image classification. *Machine Vision and Applications*, 35(4):73, 2024.
- [36] Faris Almalik, Mohammad Yaqub, and Karthik Nandakumar. Self-ensembling vision transformer (sevit) for robust medical image classification. In *International Conference on Medical Image Computing and Computer-Assisted Intervention*, pages 376–386. Springer, 2022.
- [37] Albert Gu, Karan Goel, and Christopher Ré. Efficiently modeling long sequences with structured state spaces. *arXiv preprint arXiv:2111.00396*, 2021.
- [38] Albert Gu, Isys Johnson, Karan Goel, Khaled Saab, Tri Dao, Atri Rudra, and Christopher Ré. Combining recurrent, convolutional, and continuous-time models with linear state space layers. *Advances in neural information processing systems*, 34:572–585, 2021.
- [39] Albert Gu and Tri Dao. Mamba: Linear-time sequence modeling with selective state spaces. *arXiv preprint arXiv:2312.00752*, 2023.
- [40] Jiarun Liu, Hao Yang, Hong-Yu Zhou, Yan Xi, Lequan Yu, Yizhou Yu, Yong Liang, Guangming Shi, Shaoting Zhang, Hairong Zheng, et al. Swin-umamba: Mamba-based unet with imagenet-based pretraining. *arXiv preprint arXiv:2402.03302*, 2024.
- [41] Lianghui Zhu, Bencheng Liao, Qian Zhang, Xinlong Wang, Wenyu Liu, and Xinggang Wang. Vision mamba: Efficient visual representation learning with bidirectional state space model. *arXiv preprint arXiv:2401.09417*, 2024.
- [42] Yue Liu, Yunjie Tian, Yuzhong Zhao, Hongtian Yu, Lingxi Xie, Yaowei Wang, Qixiang Ye, and Yunfan Liu. Vmamba: Visual state space model. *arXiv preprint arXiv:2401.10166*, 2024.
- [43] Keyan Chen, Bowen Chen, Chenyang Liu, Wenyuan Li, Zhengxia Zou, and Zhenwei Shi. Rsmamba: Remote sensing image classification with state space model. *IEEE Geoscience and Remote Sensing Letters*, 2024.
- [44] Zhuoran Zheng and Chen Wu. U-shaped vision mamba for single image dehazing. *arXiv preprint arXiv:2402.04139*, 2024.
- [45] Dingkan Liang, Xin Zhou, Xinyu Wang, Xingkui Zhu, Wei Xu, Zhikang Zou, Xiaoqing Ye, and Xiang Bai. Pointmamba: A simple state space model for point cloud analysis. *arXiv preprint arXiv:2402.10739*, 2024.
- [46] Jiacheng Ruan and Suncheng Xiang. Vm-unet: Vision mamba unet for medical image segmentation. *arXiv preprint arXiv:2402.02491*, 2024.
- [47] Zhaohu Xing, Tian Ye, Yijun Yang, Guang Liu, and Lei Zhu. Segmamba: Long-range sequential modeling mamba for 3d medical image segmentation. *arXiv preprint arXiv:2401.13560*, 2024.

- [48] Jun Ma, Feifei Li, and Bo Wang. U-mamba: Enhancing long-range dependency for biomedical image segmentation. *arXiv preprint arXiv:2401.04722*, 2024.
- [49] Alexander Waibel, Toshiyuki Hanazawa, Geoffrey Hinton, Kiyohiro Shikano, and Kevin J Lang. Phoneme recognition using time-delay neural networks. In *Backpropagation*, pages 35–61. Psychology Press, 2013.
- [50] Yann LeCun, Léon Bottou, Yoshua Bengio, and Patrick Haffner. Gradient-based learning applied to document recognition. *Proceedings of the IEEE*, 86(11):2278–2324, 1998.
- [51] Alex Krizhevsky, Ilya Sutskever, and Geoffrey E Hinton. Imagenet classification with deep convolutional neural networks. *Communications of the ACM*, 60(6):84–90, 2017.
- [52] Karen Simonyan and Andrew Zisserman. Very deep convolutional networks for large-scale image recognition. *arXiv preprint arXiv:1409.1556*, 2014.
- [53] Kaiming He, Xiangyu Zhang, Shaoqing Ren, and Jian Sun. Deep residual learning for image recognition. In *Proceedings of the IEEE conference on computer vision and pattern recognition*, pages 770–778, 2016.
- [54] Jiuxiang Gu, Zhenhua Wang, Jason Kuen, Lianyang Ma, Amir Shahroudy, Bing Shuai, Ting Liu, Xingxing Wang, Gang Wang, Jianfei Cai, et al. Recent advances in convolutional neural networks. *Pattern recognition*, 77:354–377, 2018.
- [55] Xia Zhao, Limin Wang, Yufei Zhang, Xuming Han, Muhammet Devenci, and Milan Parmar. A review of convolutional neural networks in computer vision. *Artificial Intelligence Review*, 57(4):99, 2024.
- [56] Saining Xie, Ross Girshick, Piotr Dollár, Zhuowen Tu, and Kaiming He. Aggregated residual transformations for deep neural networks. In *Proceedings of the IEEE conference on computer vision and pattern recognition*, pages 1492–1500, 2017.
- [57] Zhuang Liu, Hanzi Mao, Chao-Yuan Wu, Christoph Feichtenhofer, Trevor Darrell, and Saining Xie. A convnet for the 2020s. In *Proceedings of the IEEE/CVF conference on computer vision and pattern recognition*, pages 11976–11986, 2022.
- [58] François Chollet. Xception: Deep learning with depthwise separable convolutions. In *Proceedings of the IEEE conference on computer vision and pattern recognition*, pages 1251–1258, 2017.
- [59] Xiangyu Zhang, Xinyu Zhou, Mengxiao Lin, and Jian Sun. Shufflenet: An extremely efficient convolutional neural network for mobile devices. In *Proceedings of the IEEE conference on computer vision and pattern recognition*, pages 6848–6856, 2018.
- [60] Andrew G Howard, Menglong Zhu, Bo Chen, Dmitry Kalenichenko, Weijun Wang, Tobias Weyand, Marco Andreetto, and Hartwig Adam. Mobilenets: Efficient convolutional neural networks for mobile vision applications. *arXiv preprint arXiv:1704.04861*, 2017.
- [61] Yuan Liu, Ayush Jain, Clara Eng, David H Way, Kang Lee, Peggy Bui, Kimberly Kanada, Guilherme de Oliveira Marinho, Jessica Gallegos, Sara Gabriele, et al. A deep learning system for differential diagnosis of skin diseases. *Nature medicine*, 26(6):900–908, 2020.
- [62] Yifan Zhong, Chuang Cai, Tao Chen, Hao Gui, Jiajun Deng, Minglei Yang, Bentong Yu, Yongxiang Song, Tingting Wang, Xiwen Sun, et al. Pet/ct based cross-modal deep learning signature to predict occult nodal metastasis in lung cancer. *Nature Communications*, 14(1):7513, 2023.
- [63] Byungsoo Ahn, Damin Moon, Hyun-Soo Kim, Chung Lee, Nam Hoon Cho, Heung-Kook Choi, Dongmin Kim, Jung-Yun Lee, Eun Ji Nam, Dongju Won, et al. Histopathologic image-based deep learning classifier for predicting platinum-based treatment responses in high-grade serous ovarian cancer. *Nature Communications*, 15(1):4253, 2024.
- [64] Ling Dai, Bin Sheng, Tingli Chen, Qiang Wu, Ruhan Liu, Chun Cai, Liang Wu, Dawei Yang, Haslina Hamzah, Yuexing Liu, et al. A deep learning system for predicting time to progression of diabetic retinopathy. *Nature Medicine*, pages 1–11, 2024.
- [65] Alexander H Thieme, Yuanning Zheng, Gautam Machiraju, Chris Sadee, Mirja Mittermaier, Maximilian Gertler, Jorge L Salinas, Krithika Srinivasan, Prashna Gyawali, Francisco Carrillo-Perez, et al. A deep-learning algorithm to classify skin lesions from mpox virus infection. *Nature medicine*, 29(3):738–747, 2023.
- [66] Chiara Corti, Marisa Cobanaj, Edward C Dee, Carmen Criscitiello, Sara M Tolaney, Leo A Celi, and Giuseppe Curigliano. Artificial intelligence in cancer research and precision medicine: Applications, limitations and priorities to drive transformation in the delivery of equitable and unbiased care. *Cancer Treatment Reviews*, 112:102498, 2023.

- [67] Alexey Dosovitskiy, Lucas Beyer, Alexander Kolesnikov, Dirk Weissenborn, Xiaohua Zhai, Thomas Unterthiner, Mostafa Dehghani, Matthias Minderer, Georg Heigold, Sylvain Gelly, et al. An image is worth 16x16 words: Transformers for image recognition at scale. *arXiv preprint arXiv:2010.11929*, 2020.
- [68] Ibrahim Batuhan Akkaya, Senthilkumar S Kathiresan, Elahe Arani, and Bahram Zonooz. Enhancing performance of vision transformers on small datasets through local inductive bias incorporation. *Pattern Recognition*, 153:110510, 2024.
- [69] Ze Liu, Yutong Lin, Yue Cao, Han Hu, Yixuan Wei, Zheng Zhang, Stephen Lin, and Baining Guo. Swin transformer: Hierarchical vision transformer using shifted windows. In *Proceedings of the IEEE/CVF international conference on computer vision*, pages 10012–10022, 2021.
- [70] Xiaoyi Dong, Jianmin Bao, Dongdong Chen, Weiming Zhang, Nenghai Yu, Lu Yuan, Dong Chen, and Baining Guo. Cswin transformer: A general vision transformer backbone with cross-shaped windows. In *Proceedings of the IEEE/CVF conference on computer vision and pattern recognition*, pages 12124–12134, 2022.
- [71] Stéphane d’Ascoli, Hugo Touvron, Matthew L Leavitt, Ari S Morcos, Giulio Biroli, and Levent Sagun. Convit: Improving vision transformers with soft convolutional inductive biases. In *International conference on machine learning*, pages 2286–2296. PMLR, 2021.
- [72] Weihao Yu, Mi Luo, Pan Zhou, Chenyang Si, Yichen Zhou, Xinchao Wang, Jiashi Feng, and Shuicheng Yan. Metaformer is actually what you need for vision. In *Proceedings of the IEEE/CVF conference on computer vision and pattern recognition*, pages 10819–10829, 2022.
- [73] Wenhai Wang, Enze Xie, Xiang Li, Deng-Ping Fan, Kaitao Song, Ding Liang, Tong Lu, Ping Luo, and Ling Shao. Pyramid vision transformer: A versatile backbone for dense prediction without convolutions. In *Proceedings of the IEEE/CVF international conference on computer vision*, pages 568–578, 2021.
- [74] Junyu Chen, Yufan He, Eric C Frey, Ye Li, and Yong Du. Vit-v-net: Vision transformer for unsupervised volumetric medical image registration. *arXiv preprint arXiv:2104.06468*, 2021.
- [75] Onat Dalmaz, Mahmut Yurt, and Tolga Çukur. Resvit: residual vision transformers for multimodal medical image synthesis. *IEEE Transactions on Medical Imaging*, 41(10):2598–2614, 2022.
- [76] Shaoting Zhang and Dimitris Metaxas. On the challenges and perspectives of foundation models for medical image analysis. *Medical Image Analysis*, page 102996, 2023.
- [77] Michael Moor, Oishi Banerjee, Zahra Shakeri Hossein Abad, Harlan M Krumholz, Jure Leskovec, Eric J Topol, and Pranav Rajpurkar. Foundation models for generalist medical artificial intelligence. *Nature*, 616(7956):259–265, 2023.
- [78] Jun Ma, Yuting He, Feifei Li, Lin Han, Chenyu You, and Bo Wang. Segment anything in medical images. *Nature Communications*, 15(1):654, 2024.
- [79] Yukun Zhou, Mark A Chia, Siegfried K Wagner, Murat S Ayhan, Dominic J Williamson, Robbert R Struyven, Timing Liu, Moucheng Xu, Mateo G Lozano, Peter Woodward-Court, et al. A foundation model for generalizable disease detection from retinal images. *Nature*, 622(7981):156–163, 2023.
- [80] Zhi Huang, Federico Bianchi, Mert Yuksekogun, Thomas J Montine, and James Zou. A visual–language foundation model for pathology image analysis using medical twitter. *Nature medicine*, 29(9):2307–2316, 2023.
- [81] Richard J Chen, Tong Ding, Ming Y Lu, Drew FK Williamson, Guillaume Jaume, Andrew H Song, Bowen Chen, Andrew Zhang, Daniel Shao, Muhammad Shaban, et al. Towards a general-purpose foundation model for computational pathology. *Nature Medicine*, 30(3):850–862, 2024.
- [82] Jimmy TH Smith, Andrew Warrington, and Scott W Linderman. Simplified state space layers for sequence modeling. *arXiv preprint arXiv:2208.04933*, 2022.
- [83] Harsh Mehta, Ankit Gupta, Ashok Cutkosky, and Behnam Neyshabur. Long range language modeling via gated state spaces. *arXiv preprint arXiv:2206.13947*, 2022.
- [84] Daniel Y Fu, Tri Dao, Khaled K Saab, Armin W Thomas, Atri Rudra, and Christopher Ré. Hungry hungry hippos: Towards language modeling with state space models. *arXiv preprint arXiv:2212.14052*, 2022.
- [85] Md Mohaiminul Islam and Gedas Bertasius. Long movie clip classification with state-space video models. In *European Conference on Computer Vision*, pages 87–104. Springer, 2022.
- [86] Eric Nguyen, Karan Goel, Albert Gu, Gordon W Downs, Preey Shah, Tri Dao, Stephen A Baccus, and Christopher Ré. S4nd: Modeling images and videos as multidimensional signals using state spaces. *arXiv preprint arXiv:2210.06583*, 2022.

- [87] Shiyu Qin, Jinpeng Wang, Yimin Zhou, Bin Chen, Tianci Luo, Baoyi An, Tao Dai, Shutao Xia, and Yaowei Wang. Mambavc: Learned visual compression with selective state spaces. *arXiv preprint arXiv:2405.15413*, 2024.
- [88] Ningning Ma, Xiangyu Zhang, Hai-Tao Zheng, and Jian Sun. Shufflenet v2: Practical guidelines for efficient cnn architecture design. In *Proceedings of the European conference on computer vision (ECCV)*, pages 116–131, 2018.
- [89] Abien Fred Agarap. Deep learning using rectified linear units (relu). *arXiv preprint arXiv:1803.08375*, 2018.
- [90] Stefan Elfving, Eiji Uchibe, and Kenji Doya. Sigmoid-weighted linear units for neural network function approximation in reinforcement learning. *Neural networks*, 107:3–11, 2018.
- [91] Andre GC Pacheco, Gustavo R Lima, Amanda S Salomao, Breno Krohling, Igor P Biral, Gabriel G de Angelo, Fábio CR Alves Jr, José GM Esgario, Alana C Simora, Pedro BC Castro, et al. Pad-ufes-20: A skin lesion dataset composed of patient data and clinical images collected from smartphones. *Data in brief*, 32:106221, 2020.
- [92] Xavier P Burgos-Artizzu, David Coronado-Gutiérrez, Brenda Valenzuela-Alcaraz, Elisenda Bonet-Carne, Elisenda Eixarch, Fatima Crispi, and Eduard Gratacós. Evaluation of deep convolutional neural networks for automatic classification of common maternal fetal ultrasound planes. *Scientific Reports*, 10(1):10200, 2020.
- [93] Sourabh Shastri, Isha Kansal, Sachin Kumar, Kuljeet Singh, Renu Popli, and Vibhakar Mansotra. Cheximagenet: a novel architecture for accurate classification of covid-19 with chest x-ray digital images using deep convolutional neural networks. *Health and Technology*, 12(1):193–204, 2022.
- [94] Sachin Kumar, Sourabh Shastri, Shilpa Mahajan, Kuljeet Singh, Surbhi Gupta, Rajneesh Rani, Neeraj Mohan, and Vibhakar Mansotra. Litecovidnet: A lightweight deep neural network model for detection of covid-19 using x-ray images. *International Journal of Imaging Systems and Technology*, 32(5):1464–1480, 2022.
- [95] Konstantin Pogorelov, Kristin Ranheim Randel, Carsten Griwodz, Sigrun Losada Eskeland, Thomas de Lange, Dag Johansen, Concetto Spampinato, Duc-Tien Dang-Nguyen, Mathias Lux, Peter Thelin Schmidt, et al. Kvasir: A multi-class image dataset for computer aided gastrointestinal disease detection. In *Proceedings of the 8th ACM on Multimedia Systems Conference*, pages 164–169, 2017.
- [96] Xinyu Zeng, Zifan Jiang, Wen Luo, Honggui Li, Hongye Li, Guo Li, Jingyong Shi, Kangjie Wu, Tong Liu, Xing Lin, et al. Efficient and accurate identification of ear diseases using an ensemble deep learning model. *Scientific Reports*, 11(1):10839, 2021.
- [97] Jiancheng Yang, Rui Shi, Donglai Wei, Zequan Liu, Lin Zhao, Bilian Ke, Hanspeter Pfister, and Bingbing Ni. Medmnist v2-a large-scale lightweight benchmark for 2d and 3d biomedical image classification. *Scientific Data*, 10(1):41, 2023.
- [98] Jiancheng Yang, Rui Shi, and Bingbing Ni. Medmnist classification decathlon: A lightweight automl benchmark for medical image analysis. In *2021 IEEE 18th International Symposium on Biomedical Imaging (ISBI)*, pages 191–195. IEEE, 2021.
- [99] Ilya Loshchilov and Frank Hutter. Decoupled weight decay regularization. *arXiv preprint arXiv:1711.05101*, 2017.
- [100] Ekin D Cubuk, Barret Zoph, Dandelion Mane, Vijay Vasudevan, and Quoc V Le. Autoaugment: Learning augmentation strategies from data. In *Proceedings of the IEEE/CVF conference on computer vision and pattern recognition*, pages 113–123, 2019.
- [101] Xiaohan Ding, Xiangyu Zhang, Ningning Ma, Jungong Han, Guiguang Ding, and Jian Sun. Repvgg: Making vgg-style convnets great again. In *Proceedings of the IEEE/CVF conference on computer vision and pattern recognition*, pages 13733–13742, 2021.
- [102] Sachin Mehta and Mohammad Rastegari. Separable self-attention for mobile vision transformers. *arXiv preprint arXiv:2206.02680*, 2022.
- [103] Muhammad Maaz, Abdelrahman Shaker, Hisham Cholakkal, Salman Khan, Syed Waqas Zamir, Rao Muhammad Anwer, and Fahad Shahbaz Khan. Edgenext: efficiently amalgamated cnn-transformer architecture for mobile vision applications. In *European Conference on Computer Vision*, pages 3–20. Springer, 2022.
- [104] Zizhao Zhang, Han Zhang, Long Zhao, Ting Chen, Sercan Ö Arik, and Tomas Pfister. Nested hierarchical transformer: Towards accurate, data-efficient and interpretable visual understanding. In *Proceedings of the AAAI Conference on Artificial Intelligence*, volume 36, pages 3417–3425, 2022.
- [105] Pavan Kumar Anasosalu Vasu, James Gabriel, Jeff Zhu, Oncel Tuzel, and Anurag Ranjan. Mobileone: An improved one millisecond mobile backbone. In *Proceedings of the IEEE/CVF conference on computer vision and pattern recognition*, pages 7907–7917, 2023.

- [106] Hugo Touvron, Matthieu Cord, Alexandre Sablayrolles, Gabriel Synnaeve, and Hervé Jégou. Going deeper with image transformers. In *Proceedings of the IEEE/CVF international conference on computer vision*, pages 32–42, 2021.
- [107] Gao Huang, Zhuang Liu, Laurens Van Der Maaten, and Kilian Q Weinberger. Densely connected convolutional networks. In *Proceedings of the IEEE conference on computer vision and pattern recognition*, pages 4700–4708, 2017.
- [108] Weihao Yu, Chenyang Si, Pan Zhou, Mi Luo, Yichen Zhou, Jiashi Feng, Shuicheng Yan, and Xinchao Wang. Metaformer baselines for vision. *IEEE Transactions on Pattern Analysis and Machine Intelligence*, 2023.
- [109] Kai Han, An Xiao, Enhua Wu, Jianyuan Guo, Chunjing Xu, and Yunhe Wang. Transformer in transformer. *Advances in neural information processing systems*, 34:15908–15919, 2021.
- [110] Wenhai Wang, Enze Xie, Xiang Li, Deng-Ping Fan, Kaitao Song, Ding Liang, Tong Lu, Ping Luo, and Ling Shao. Pvt v2: Improved baselines with pyramid vision transformer. *Computational Visual Media*, 8(3):415–424, 2022.
- [111] Mingyu Ding, Bin Xiao, Noel Codella, Ping Luo, Jingdong Wang, and Lu Yuan. Davit: Dual attention vision transformers. In *European conference on computer vision*, pages 74–92. Springer, 2022.
- [112] Hugo Touvron, Matthieu Cord, Matthijs Douze, Francisco Massa, Alexandre Sablayrolles, and Hervé Jégou. Training data-efficient image transformers & distillation through attention. In *International conference on machine learning*, pages 10347–10357. PMLR, 2021.
- [113] Mingxing Tan and Quoc Le. Efficientnetv2: Smaller models and faster training. In *International conference on machine learning*, pages 10096–10106. PMLR, 2021.
- [114] Weijian Xu, Yifan Xu, Tyler Chang, and Zhuowen Tu. Co-scale conv-attentional image transformers. In *Proceedings of the IEEE/CVF international conference on computer vision*, pages 9981–9990, 2021.
- [115] Yanghao Li, Chao-Yuan Wu, Haoqi Fan, Karttikeya Mangalam, Bo Xiong, Jitendra Malik, and Christoph Feichtenhofer. Mvitv2: Improved multiscale vision transformers for classification and detection. In *Proceedings of the IEEE/CVF Conference on Computer Vision and Pattern Recognition*, pages 4804–4814, 2022.
- [116] Mingxing Tan and Quoc Le. Efficientnet: Rethinking model scaling for convolutional neural networks. In *International conference on machine learning*, pages 6105–6114. PMLR, 2019.
- [117] Jianwei Yang, Chunyuan Li, Xiyang Dai, and Jianfeng Gao. Focal modulation networks. *Advances in Neural Information Processing Systems*, 35:4203–4217, 2022.
- [118] Xiangxiang Chu, Zhi Tian, Yuqing Wang, Bo Zhang, Haibing Ren, Xiaolin Wei, Huaxia Xia, and Chunhua Shen. Twins: Revisiting the design of spatial attention in vision transformers. *Advances in neural information processing systems*, 34:9355–9366, 2021.
- [119] Weihao Yu, Mi Luo, Pan Zhou, Chenyang Si, Yichen Zhou, Xinchao Wang, Jiashi Feng, and Shuicheng Yan. Metaformer is actually what you need for vision. In *Proceedings of the IEEE/CVF conference on computer vision and pattern recognition*, pages 10819–10829, 2022.
- [120] Alaaeldin Ali, Hugo Touvron, Mathilde Caron, Piotr Bojanowski, Matthijs Douze, Armand Joulin, Ivan Laptev, Natalia Neverova, Gabriel Synnaeve, Jakob Verbeek, et al. Xcit: Cross-covariance image transformers. *Advances in neural information processing systems*, 34:20014–20027, 2021.
- [121] Ali Hatamizadeh, Hongxu Yin, Greg Heinrich, Jan Kautz, and Pavlo Molchanov. Global context vision transformers. In *International Conference on Machine Learning*, pages 12633–12646. PMLR, 2023.
- [122] Matthias Feurer, Aaron Klein, Katharina Eggenberger, Jost Springenberg, Manuel Blum, and Frank Hutter. Efficient and robust automated machine learning. *Advances in neural information processing systems*, 28, 2015.
- [123] Haifeng Jin, Qingquan Song, and Xia Hu. Auto-keras: An efficient neural architecture search system. In *Proceedings of the 25th ACM SIGKDD international conference on knowledge discovery & data mining*, pages 1946–1956, 2019.
- [124] Ekaba Bisong and Ekaba Bisong. Google automl: cloud vision. *Building Machine Learning and Deep Learning Models on Google Cloud Platform: A Comprehensive Guide for Beginners*, pages 581–598, 2019.
- [125] Ramprasaath R Selvaraju, Michael Cogswell, Abhishek Das, Ramakrishna Vedantam, Devi Parikh, and Dhruv Batra. Grad-cam: Visual explanations from deep networks via gradient-based localization. In *Proceedings of the IEEE international conference on computer vision*, pages 618–626, 2017.
- [126] Chak Fong Chong, Xinyi Fang, Xu Yang, Wuman Luo, and Yapeng Wang. On the correlations between performance of deep networks and its robustness to common image perturbations in medical image interpretation. In *2023 International Conference on Digital Image Computing: Techniques and Applications (DICTA)*, pages 426–433. IEEE, 2023.

- [127] Tim JM Jaspers, Tim GW Boers, Carolus HJ Kusters, Martijn R Jong, Jelmer B Jukema, Albert J de Groof, Jacques J Bergman, Peter HN de With, and Fons van der Sommen. Robustness evaluation of deep neural networks for endoscopic image analysis: Insights and strategies. *Medical Image Analysis*, 94:103157, 2024.
- [128] Albert T Young, Kristen Fernandez, Jacob Pfau, Rasika Reddy, Nhat Anh Cao, Max Y von Franque, Arjun Johal, Benjamin V Wu, Rachel R Wu, Jennifer Y Chen, et al. Stress testing reveals gaps in clinic readiness of image-based diagnostic artificial intelligence models. *NPJ digital medicine*, 4(1):10, 2021.